J. Am. Chem. Soc. **1994,** *116,* 9071–9085

Monomeric Carboxylate Ferrous Complexes as Models for the Dioxygen Binding Sites in Non-Heme Iron Proteins. The Reversible Formation and Characterization of μ-Peroxo Diferric Complexes

Nobumasa Kitajima,[*,1] Nobuchika Tamura,[1] Hironobu Amagai,[1] Hideno Fukui,[1] Yoshihiko Moro-oka,[*,1] Yasuhisa Mizutani,[2] Teizo Kitagawa,[2] Rajeev Mathur,[3] Kristel Heerwegh,[3] Christopher A. Reed,[*,3] Clayton R. Randall,[4] Lawrence Que, Jr.,[*,4] and Kazuyuki Tatsumi[*,5]

Contribution from the Research Laboratory of Resources Utilization, Tokyo Institute of Technology, 4259 Nagatsuta, Yokohama 227, Japan, the Institute for Molecular Science, Okazaki National Research Institutes and the Department of Functional Molecular Science, Graduate University for Advanced Studies, Myodaiji, Okazaki 444, Japan, the Department of Chemistry, University of Southern California, Los Angeles, California 90089-0744, the Department of Chemistry, University of Minnesota, 207 Pleasant Street S.E., Minneapolis, Minnesota 55455-0431, and the Department of Chemistry, Faculty of Science, Nagoya University, Chikusa, Nagoya 464-01, Japan

Received January 13, 1994[•]

Abstract: A series of monomeric carboxylate ferrous complexes with a tripodal N_3 ligand $HB(3,5\text{-}iPr_2pz)_3$ has been synthesized and characterized to model the iron site in non-heme iron proteins which bind or activate dioxygen. The structures of $Fe(OAc)(HB(3,5\text{-}iPr_2pz)_3)$ (**2**), $Fe(OBz)(MeCN)(HB(3,5\text{-}iPr_2pz)_3)$ (**3**), and $Fe(OOCtBu)(HB(3,5\text{-}iPr_2pz)_3)$ (**13**) were determined by X-ray crystallography. The five-coordinate complex $Fe(OBz)(HB(3,5\text{-}iPr_2pz)_3)$ (**4**) was found to bind a variety of σ-donating ligands such as dimethyl sulfoxide and pyridine at the open coordination site. The reaction between the ferrous complexes and dioxygen has been explored. $Fe(OBz)(HB(3,5\text{-}iPr_2pz)_3)$ (**4**) was found to bind dioxygen to form an adduct which is reasonably stable below −20 °C. The dioxygen adduct was characterized by dioxygen uptake measurement, and UV–vis, resonance Raman, ^1H-NMR, and X-ray absorption spectroscopy. On the basis of these results, the $Fe:O_2$ stoichiometry of 2:1, an intense absorption band at 682 nm, $\nu(O–O)$ at 876 cm^{-1}, and $Fe\cdots Fe$ separation of 4.3 Å estimated from EXAFS, the dioxygen adduct was identifed as a μ-peroxo dinuclear ferric complex. The variable temperature magnetic susceptibility measurement of the isolated μ-peroxo complex indicates that the complex is antiferromagnetically coupled with $J = -33$ cm^{-1}, which is weaker than those known for other μ-peroxo dinuclear ferric complexes. This characteristic feature may be associated with the structurally unique Fe–O–O–Fe frame, which is discussed on the basis of the extended Hückel calculations. Above −20 °C, the reaction of **4** with dioxygen causes irreversible oxidation, resulting in formation of a trimeric ferric complex $(HB(3,5\text{-}iPr_2pz)_3)Fe(OBz)_2(O)Fe(OH)(OBz)_2Fe(HB(3,5\text{-}iPr_2pz)_3)$ (**16**). This assignment is consistent with the magnetic property, Mössbauer spectrum, and X-ray analysis.

Introduction

The binding of dioxygen at a ferrous site in proteins is an indispensable step in a variety of physiologically important reactions involved in dioxygen metabolism, e.g., the reversible binding of dioxygen and the mono- or dioxygenation of organic compounds. The most extensively studied and characterized class of such proteins are hemoproteins including hemoglobin[6] and cytochrome P-450.[7] A huge body of information on the detailed active site structures and the functional roles of the heme in binding and/or activating dioxygen has been provided.[8] In contrast, many aspects of the structures and mechanisms of non-heme iron proteins known to interact with dioxygen remain to be elucidated.

A class of non-heme iron proteins whose active site consists of a pair of iron centers has recently emerged.[9–14] The unique structural and spectral features of the diiron sites have attracted much attention. The prototype protein in this class is hemerythrin, a dioxygen carrier for some marine worms. The active site structure and the mechanism of dioxygen binding in hemerythrin has been studied extensively.[10] Other examples of this class capable of activating dioxygen include methane monooxygenase[11]

[•] Abstract published in *Advance ACS Abstracts,* August 15, 1994.

(1) Tokyo Institute of Technology.

(2) Institute for Molecular Science.

(3) University of Southern California.

(4) University of Minnesota.

(5) Nagoya University.

(6) (a) Perutz, M. F. *Annu. Rev. Biochem.* **1979,** *48,* 327. (b) Dickerson, R. E.; Geis, I. *Hemoglobin: Structure, Function, Evolution and Pathology*; Benjamin/Cummings: Menlo Park, 1983.

(7) (a) White, R. E.; Coon, M. J. *Annu. Rev. Biochem.* **1980,** *49,* 315. (b) Guengerich, F. P.; Macdonald, T. L. *Acc. Chem. Res.* **1984,** *17,* 9. (c) Oriz de Montellano, P. R., Ed. *Cytochrome P-450, Structure, Mechanism and Biochemistry*; Plenum: New York, 1986.

(8) (a) Jones, R. D.; Summerville, D. A.; Basolo, F. *Chem. Rev.* **1979,** *79,* 139. (b) Collman, J. P.; Halbert, T. R.; Suslick, K. S. In *Metal Iron Activation of Dioxygen*; Spiro, T. G., Ed.; John Wiley and Sons: New York, 1980; p 1.

(9) Sanders-Loehr, J. *Iron Carriers and Iron Proteins*; Loehr, T. M., Ed.; VCH: New York, 1989; p 373.

(10) (a) Sanders-Loehr, J.; Loehr, T. M. *Adv. Inorg. Biochem.* **1979,** *1,* 235. (b) Klotz, I. M.; Kurtz, D. M., Jr. *Acc. Chem. Res.* **1984,** *17,* 16. (c) Wilkins, P. C.; Wilkins, R. G. *Coord. Chem. Rev.* **1987,** *79,* 195.

(11) (a) Higgins, I. J.; Best, D. J.; Hammond, R. C. *Nature* (*London*) **1980,** *286,* 561. (b) Higgins, I. J.; Best, D. J.; Hammond, R. C.; Scott, D. *Microbiol. Rev.* **1981,** *45,* 556. (c) Dalton, H. *Adv. Appl. Microbiol.* **1980,** *26,* 71. (d) Fox, B. G.; Froland, W. A.; Dege, J. E.; Lipscomb, J. D. *J. Biol. Chem.* **1989,** *264,* 10023. (e) Rosenzweig, A. C.; Frederick, C. A.; Lippard, S. J.; Nordlund, P. *Nature* (*London*) **1993,** *366,* 537.

(12) (a) Sjöberg, B.-M.; Gräslund, A. *Adv. Inorg. Biochem.* **1983,** *5,* 87. (b) Nordlund, P.; Sjöberg, B.-M.; Eklund, H. *Nature* (*London*) **1990,** *345,* 593. (c) Nordlund, P.; Eklund, P.; Eklund, H. *J. Mol. Biol.* **1993,** *232,* 123.

(13) Antanaitis, B. C.; Aisen, P. *Adv. Inorg. Biochem.* **1983,** *5,* 111.

(14) LeGall, J.; Prickril, B. C.; Moura, I.; Xavier, A. V.; Moura, J. J. G.; Huynh, B.-H. *Biochemistry* **1988,** *27,* 1636.

0002-7863/94/1516-9071$04.50/0

and ribonucleotide reductase[12] whose X-ray structures have been reported recently. The synthesis of dinuclear ferric complexes to structurally mimic the active sites of these proteins has been the subject of numerous investigations.[15] These synthetic endeavors have provided a solid inorganic and physicochemical basis for understanding the precise electronic structures of the diferric (or met) states of hemerythrin and other proteins. However, only a few diferrous complexes modeling the reduced states of the diiron sites have been reported to date.[16–23] Although these complexes mimic some of the structural features or magnetic properties of the proteins, only two of these form dioxygen adducts stable enough to be characterized by spectroscopic means; in both cases, formation of a *cis*-μ-peroxo diferric complex was demonstrated by resonance Raman spectroscopy.[21,22]

Besides the above mentioned non-heme iron proteins containing dinuclear sites, a variety of mononuclear non-heme iron enzymes are known. Exemplified are iron superoxide dismutase,[24] phenylalanine hydroxylase,[25] tyrosine hydroxylase,[26] ω-hydroxylase,[27] catechol dioxygenase,[28] benzene dioxygenase,[29] and lipoxygenase.[30] Among these proteins, the X-ray structures of only three have been reported: iron superoxide dismutase,[31] protocatechuate 3,4-dioxygenase,[32] and lipoxygenase.[33] The active site structures of the other proteins remain to be elucidated. The dioxygen chemistry of mononuclear ferrous complexes having non-porphyrinic ligands may shed light on the structural factors that differentiate the specific functions of the non-heme iron proteins. Previous studies along this line include investigations of mononuclear ferrous complexes with macrocyclic N ligands by Baldwin,[34] Busch,[35] and Kimura.[36] However, the strong tetragonality of the ligand systems employed in these studies resulted in chemistry more closely associated with that of heme rather than non-heme iron proteins.

Recently, some of us communicated the synthesis and structure of a mononuclear benzoate ferrous complex with the tripodal capping ligand HB(3,5-iPr$_2$pz)$_3$.[37,38] The complex was designed to structurally mimic the iron site responsible for dioxygen binding in hemerythrin and the mononuclear site in iron superoxide dismutase. In the former case, dioxygen is known to be bound to only one of the two ferrous irons which is five coordinate with a N_2O_3 ligand donor set consisting of histidyl nitrogen and carboxylate oxygen.[10] The active site structure of iron superoxide dismutase is best described as a distorted tetrahedral surrounded by N_3O_1 ligand donors from histidine and aspartate.[31] In addition, the ferrous ion in reduced lipoxygenase is found to be supported by three histidines and one isoleucine.[33] Thus, the structure of the five-coordinate benzoate complex is, to some extent, similar to the dioxygen binding sites in these proteins, and possibly those of other non-heme iron proteins. In the present study, a series of carboxylate complexes Fe(OOCR)(HB(3,5-iPr$_2$pz)$_3$) was synthesized and their reactivities toward dioxygen were explored in detail.

Results and Discussion

Synthesis of Monomeric Carboxylate Ferrous Complexes. The ligand displacement reaction of a ferrous chloro complex Fe(Cl)(HB(3,5-iPr$_2$pz)$_3$)[39] (**1**) and NaOOCR yielded a monomeric carboxylate ferrous complex Fe(OOCR)(HB(3,5-iPr$_2$pz)$_3$) (eq 1). A variety of carboxylate complexes were synthesized in this manner and their structures were established by elemental analysis and IR and ^{1}H-NMR spectroscopy as described in the Experimental Section. For instance, the reaction of **1** with 1.5 equiv of NaOAc afforded Fe(OAc)(HB(3,5-iPr$_2$pz)$_3$) (**2**) essentially in quantitative yield. Figure 1 represents the ^{1}H-NMR spectrum of **2** recorded at room temperature. The assignment of the signals was based on the integrated intensities of the signals and by labeling experiments; the corresponding signals due to the pyrazole 4-position and the hydride on boron were not observed for Fe(OBz)(HB(3,5-iPr$_2$-4-Brpz)$_3$) (**5**) and Fe(OOCC$_6$H$_4$-*p*-NO$_2$)(DB(3,5-iPr$_2$pz)$_3$) (**7**), respectively (see the Experimental Section). The observed signals span the range of -10 to $+115$ ppm, indicative of a high-spin ferrous ion in **2**.

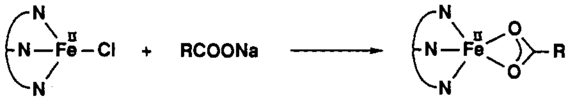

(1)

X-ray-quality single crystals of **2** were obtained by slow recrystallization from pentane. The crystal structure is presented in Figure 2 and selected bond distances and bond angles are summarized in Table 1. Complex **2** is monomeric with a

---

(15) (a) Lippard, S. J. *Angew. Chem., Int. Ed. Engl.* **1988**, *27*, 344. (b) Kurtz, D. M., Jr. *Chem. Rev.* **1990**, *90*, 585. (c) Que, L., Jr.; True, A. E. *Prog. Inorg. Chem.* **1990**, *38*, 97.

(16) Hartman, J. R.; Rardin, R. L.; Chaudhuri, P.; Pohl, K.; Wieghardt, K.; Nuber, B.; Weiss, J.; Papaefthymiou, G. C.; Frankel, R. B.; Lippard, S. J. *J. Am. Chem. Soc.* **1987**, *109*, 7387.

(17) Borovik, A. S.; Hendrich, M. P.; Holman, T. R.; Münck, E.; Papaefthymiou, V.; Que, L., Jr. *J. Am. Chem. Soc.* **1990**, *112*, 6031.

(18) Tolman, W. B.; Liu, S.; Bentsen, J. G.; Lippard, S. J. *J. Am. Chem. Soc.* **1991**, *113*, 152.

(19) Stassinopoulos, A.; Schulte, G.; Papaefthymiou, G. C.; Caradonna, J. P. *J. Am. Chem. Soc.* **1991**, *113*, 8686.

(20) Ménage, S.; Zang, Y.; Hendrich, M. P.; Que, L., Jr. *J. Am. Chem. Soc.* **1992**, *114*, 7786.

(21) (a) Ménage, S.; Brennan, B. A.; Juarez-Garcia, C.; Münck, E.; Que, L., Jr. *J. Am. Chem. Soc.* **1990**, *112*, 6423. (b) Dong, Y.; Ménage, S.; Brennan, B. A.; Elgren, T. E.; Jang, H. G.; Pearce, L. L.; Que, L., Jr. *J. Am. Chem. Soc.* **1993**, *115*, 1851.

(22) Hayashi, Y.; Suzuki, M.; Uehara, A.; Mizutani, Y.; Kitagawa, T. *Chem. Lett.* **1992**, *91*.

(23) Kitajima, N.; Tamura, N.; Tanaka, M.; Moro-oka, Y. *Inorg. Chem.* **1992**, *31*, 3342.

(24) (a) Fridovich, I. *Acc. Chem. Res.* **1982**, *15*, 200. (b) Valentine, J. S.; Pantoliano, M. W. *Copper Proteins*; Spiro, T. G., Ed.; Wiley: New York, 1981; p 291.

(25) (a) Dix, T. A.; Bollag, G. E.; Domanico, P. L.; Benkovic, S. J. *Biochemistry* **1985**, *24*, 2955. (b) Dix, T. A.; Benkovic, S. J. *Biochemistry* **1985**, *24*, 5839. (c) Benkovic, S. J.; Bloom, L. M.; Bollag, G.; Dix, T. A.; Gaffney, B. J.; Pember, S. *Ann. N.Y. Acad. Sci.* **1986**, *471*, 226.

(26) (a) Dix, T. A.; Kuhn, D. M.; Benkovic, S. J. *Biochemistry* **1987**, *26*, 3354. (b) Andersson, K. K.; Cox, D. D.; Que, L., Jr.; Flatmark, T.; Haavik, J. *J. Biol. Chem.* **1988**, *263*, 18621.

(27) (a) Ruettinger, R. T.; Griffith, G. R.; Coon, M. J. *Arch. Biochem. Biophys.* **1977**, *183*, 528. (b) Katopodis, A. G.; Wimalasena, K.; Lee, J.; May, S. W. *J. Am. Chem. Soc.* **1984**, *106*, 7928.

(28) Que, L., Jr. *Iron Carriers and Iron Proteins*; Loehr, T. M., Ed., VCH: New York, 1989; p 467.

(29) (a) Crutcher, S. E.; Geary, P. J. *Biochem. J.* **1979**, *177*, 393. (b) Geary, P. J.; Dickson, D. P. E. *Biochem. J.* **1981**, *195*, 199.

(30) (a) Veldink, G. A.; Vliegenthart, J. F. G. *Adv. Inorg. Biochem.* **1984**, *6*, 139. (b) Nelson, M. J.; Cowling, R. A. *J. Am. Chem. Soc.* **1990**, *112*, 2820.

(31) (a) Ringe, D.; Petsko, G. A.; Yamakura, F.; Suzuki, K.; Ohmori, D. *Proc. Natl. Acad. Sci. U.S.A.* **1983**, *80*, 3879. (b) Stallings, W. C.; Powers, T. B.; Pattridge, K. A.; Fee, J. A.; Ludwig, M. L. *Proc. Natl. Acad. Sci. U.S.A.* **1983**, *80*, 3884. (c) Stoddard, B. L.; Howell, P. L.; Ringe, D.; Petsko, G. A. *Biochemistry* **1990**, *29*, 8885.

(32) (a) Ohlendorf, D. H.; Weber, P. C.; Lipscomb, J. D. *J. Mol. Biol.* **1987**, *195*, 225. (b) Ohlendorf, D. H.; Lipscomb, J. D.; Weber, P. C. *Nature (London)* **1988**, *336*, 403.

(33) (a) Boyington, J. C.; Gaffney, B. J.; Amzel, L. M. *Science* **1993**, *260*, 1482. (b) Minor, W.; Steczko, J.; Bolin, J. T.; Otwinowski, Z.; Axelrod, B. *Biochemistry* **1993**, *32*, 6320.

(34) Baldwin, J. E.; Huff, J. *J. Am. Chem. Soc.* **1973**, *95*, 5757.

(35) Herron, N.; Cameron, J. H.; Neer, G. L.; Busch, D. H. *J. Am. Chem. Soc.* **1983**, *105*, 298.

(36) Kimura, E.; Kodama, M.; Machida, R.; Ishizu, K. *Inorg. Chem.* **1982**, *21*, 595.

(37) Kitajima, N.; Fukui, H.; Moro-oka, Y.; Mizutani, Y.; Kitagawa, T. *J. Am. Chem. Soc.* **1990**, *112*, 6402.

(38) Abbreviations used are as follows: HB(3,5-iPr$_2$pz)$_3$, hydrotris(3,5-diisopropylpyrazol-1-yl)borate(1−); OBz, benzoate; OAc, acetate; OOCtBu, pivalate; OOCAd, 1-adamantylcarboxylate; acac, acetylacetonate; BPMP, 2,6-bis[[bis(2-pyridylmethyl)amino]methyl]-4-methylphenolate; TMPA, tris(2-pyridylmethyl)amine; Me$_3$TACN, 1,4,7-trimethyl-1,4,7-triazacyclononane; TPP, *meso*-tetra-*p*-tolylporphyrin; *p*-OMe-TPP, tetra(*p*-methoxyphenyl)porphyrin; HPTB, *N,N,N′,N′*-tetrakis(benzimidazol-2-ylmethyl)-1,3-diaminopropan-2-olate; *N*-Et-HPTB, *N,N,N′,N′*-tetrakis[(*N*-ethylbenzimidazol-2-yl)methyl]-1,3-diaminopropan-2-olate; tpdp, *N,N,N′,N′*-tetraks[(6-methylpyrid-2-yl)methyl]-1,3-diaminopropan-2-olate; EXAFS, extended X-ray absorption fine structure; XANES, X-ray absorption near-edge structure.

(39) Kitajima, N.; Ito, M.; Amagai, H.; Moro-oka, Y. Manuscript in preparation.

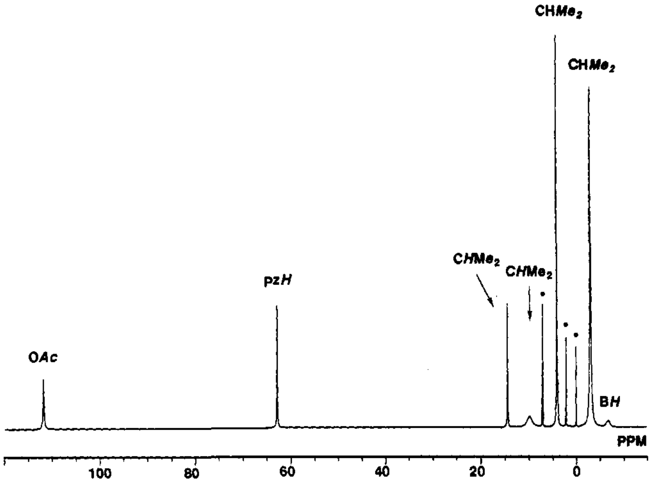

Figure 1. ^{1}H-NMR spectrum (270 MHz) of Fe(OAc)(HB(3,5-iPr$_2$pz)$_3$) (**2**) in toluene-d_8 at 27 °C. Peaks labeled with an asterisk are due to solvents.

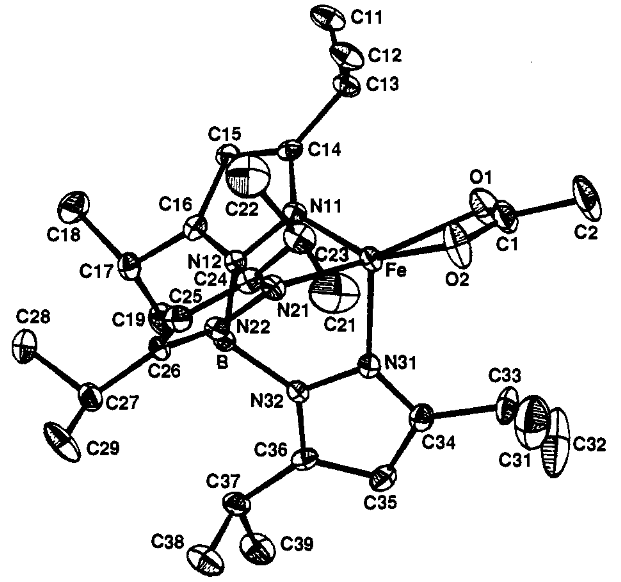

Figure 2. ORTEP view of Fe(OAc)(HB(3,5-iPr$_2$pz)$_3$) (**2**).

Table 1. Selected Bond Distances (Å) and Angles (Deg) for Fe(OAc)(HB(3,5-iPr$_2$pz)$_3$) (**2**)

	Bond Distances		
Fe–O1	2.234(3)	N11–N12	1.376(3)
Fe–O2	2.060(3)	N12–B	1.555(4)
Fe–N11	2.073(3)	N21–N22	1.384(4)
Fe–N21	2.093(2)	N22–B	1.538(4)
Fe–N31	2.092(3)	N31–N32	1.371(3)
O1–C1	1.230(5)	N32–B	1.556(4)
O2–C1	1.268(5)	C1–C2	1.506(5)
	Bond Angles		
O1–Fe–O2	60.2(1)	Fe–N11–N12	115.0(2)
O1–Fe–N11	103.5(1)	N11–N12–B	119.7(2)
O1–Fe–N21	160.6(1)	Fe–N21–N22	114.9(2)
O1–Fe–N31	104.5(1)	N21–N22–B	119.3(2)
O2–Fe–N11	150.5(1)	Fe–N31–N32	115.7(2)
O2–Fe–N21	103.3(1)	N31–N32–B	118.9(2)
O2–Fe–N31	115.8(1)	N12–B–N22	110.1(2)
N11–Fe–N21	86.4(1)	N12–B–N32	109.4(3)
N11–Fe–N31	91.4(1)	N22–B–N32	109.4(3)
N21–Fe–N31	91.7(1)	O1–C1–O2	119.7(3)
Fe–O1–C1	86.5(2)	O1–C1–C2	120.5(4)
Fe–O2–C1	93.5(3)	O2–C1–C2	119.8(4)

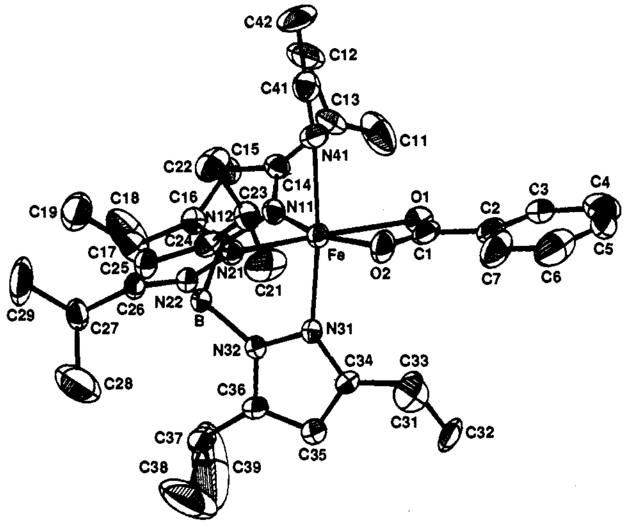

Figure 3. ORTEP view of Fe(OBz)(MeCN)(HB(3,4-iPr$_2$pz)$_3$) (**3**).

coordination structure best described as square pyramidal with one nitrogen (N31) from the tris(pyrazolyl)borate ligand as an apical ligand. The acetate group is bound to the iron in an unsymmetric bidentate fashion, and the two oxygen donors together with two nitrogens from the tris(pyrazolyl)borate ligand form the basal plane. The site opposite to the apical nitrogen is vacant and effectively shielded by two isopropyl groups.

Formation of Adducts with σ-Donor Ligands. When the five-coordinate complexes Fe(OAc)(HB(3,5-iPr$_2$pz)$_3$) (**2**) and Fe(OBz)(HB(3,5-iPr$_2$pz)$_3$) (**4**) were recrystallized from acetonitrile, the crystals formed were found to contain the solvent, which is easily lost when exposed to the air. Coordination of acetonitrile to iron is suggested from the sharp absorption band observed at 2277 cm^{-1}, attributable to ν(CN) of the coordinated acetonitrile; free acetonitrile gives the band at 2255 cm^{-1}. The X-ray analysis of the acetonitrile adduct of **4** established definitely a distorted octahedral structure with one coordinated acetonitrile molecule. The ORTEP view of the adduct Fe(OBz)(MeCN)(HB(3,5-iPr$_2$pz)$_3$) (**3**) is shown in Figure 3. The acetonitrile molecule occupies the open coordination site of **4**. The benzoate group coordinates to the iron in a slightly unsymmetrical bidentate fashion while its distortion is less than that found in **2**. Two carboxylate oxygen atoms and two nitrogen atoms from the tris(pyrazolyl)borate ligand constitute a basal plane. The geometry around the iron is close to a regular octahedron but is slightly distorted. Thus, the bond distances between the iron and the apical nitrogens, N31 and N41, are distinctly more elongated than those between the iron and the basal oxygen or nitrogen atoms (see Table 2).

The formation of six-coordinate adducts of **4** with a variety of σ-donor ligands other than acetonitrile was explored in detail by ^{1}H-NMR. Table 3 compares the chemical shift values of **4** in the presence of 1 equiv of the externally added ligand. The spectra were recorded at 27 °C in benzene-d_6. No significant change in the spectrum was observed upon the addition of trimethylphosphine, triphenylphosphine, or triethylamine, suggesting no significant interaction between **4** and these ligands. Since the change of the spectrum upon the addition of acetonitrile is also negligible despite the evident adduct formation, we evaluated the formation of adducts by FD-MS spectroscopy, which provided negative evidence. No interaction between **4** and trimethylphosphine, triphenylphosphine, and triethylamine can be ascribed to the steric bulk of these substrates. It is also evident that acetonitrile is rather weakly bound to **4** forming a 1:1 adduct only partially under this reaction condition, accounting for the small change of the ^{1}H-NMR spectrum. With other ligands, the overall features of the spectra changed, consistent with coordination to the vacant site of **4**. In particular, striking shifts of the proton signals are observed upon the addition of pyridine and dimethyl sulfoxide. Because both ligands are strong σ-donors, it is suggested that the predominant interaction between the iron and an

Table 2. Selected Bond Distances (Å) and Angles (Deg) for $Fe(OBz)(MeCN)(HB(3,5\text{-}iPr_2pz)_3)$ (**3**)

	Bond Distances		
Fe–O1	2.252(8)	N31–N32	1.37(1)
Fe–O2	2.135(8)	N32–B	1.57(1)
Fe–N11	2.116(7)	N41–C41	1.13(2)
Fe–N21	2.118(7)	C1–C2	1.52(2)
Fe–N31	2.196(7)	C2–C3	1.34(2)
Fe–N41	2.276(9)	C2–C7	1.39(2)
O1–C1	1.28(2)	C3–C4	1.45(3)
O2–C1	1.22(2)	C4–C5	1.30(3)
N11–N12	1.38(1)	C5–C6	1.47(3)
N12–B	1.55(1)	C6–C7	1.42(2)
N21–N22	1.37(1)	C41–C42	1.52(2)
N22–B	1.55(1)		
	Bond Angles		
O1–Fe–O2	59.2(3)	N21–N22–B	119.9(7)
O1–Fe–N11	105.9(3)	Fe–N31–N32	114.5(5)
O1–Fe–N21	161.9(3)	N31–N32–B	120.4(7)
O1–Fe–N31	99.1(3)	Fe–N41–C41	172.4(9)
O1–Fe–N41	86.1(3)	N12–B–N22	111.0(7)
O2–Fe–N11	164.3(3)	N12–B–N32	108.8(8)
O2–Fe–N21	103.0(3)	N22–B–N32	108.3(8)
O2–Fe–N31	99.2(3)	O1–C1–O2	121(1)
O2–Fe–N41	86.0(3)	O1–C1–C2	118(1)
N11–Fe–N21	91.7(3)	O2–C1–C2	121(1)
N11–Fe–N31	87.3(3)	C1–C2–C3	123(1)
N11–Fe–N41	88.4(3)	C1–C2–C7	115(1)
N21–Fe–N31	85.8(3)	C3–C2–C7	115(1)
N21–Fe–N41	90.2(3)	C2–C3–C4	123(2)
N31–Fe–N41	174.0(3)	C3–C4–C5	112(2)
Fe–O1–C1	86.4(7)	C4–C5–C6	131(2)
Fe–O2–C1	93.4(7)	C5–C6–C7	112(2)
Fe–N11–N12	115.9(5)	C2–C7–C6	120(2)
N11–N12–B	120.6(7)	N41–C41–C42	178(1)
Fe–N21–N22	117.0(6)		

externally added ligand is associated with the σ-donation from the ligand to the ferrous ion and that the contribution of π-back bonding is negligible. This interpretation is supported by the observation that the coordinated acetonitrile exhibits ν(CN) at higher energy than that of free acetonitrile as described above. Similarly, ν(CN) of the *n*-butyl isocyanide adduct also shifts to higher energy (2166 vs 2148 cm^{-1} for free *n*-butyl isocyanide).

The binding constant of pyridine to **4** was determined from the dependence of the chemical shift of the 4-pyrazole proton upon the concentration of pyridine. Representative ^{1}H-NMR spectra are given in Figure 4. The resonance attributable to the pyrazole 4-proton is shifted to higher field with increasing amounts of added pyridine. Given the binding/dissociation equilibrium between **4** and the pyridine adduct as eq 2, derived is eq 3.

$$\mathrm{LFe(OBz)} + \mathrm{Py} \overset{K}{\rightleftharpoons} \mathrm{LFe(OBz)(Py)} \qquad (2)$$

$$1/(\delta - \delta_2) = 1/(\delta_1 - \delta_2) + K[\mathrm{Py}]/(\delta_1 - \delta_2) \qquad (3)$$

$$\delta = \delta_1 x + \delta_2 y \qquad (4)$$

$$x = [\mathrm{LFe(OBz)}]/[\mathrm{LFe(OBz)}]_0 \quad y = [\mathrm{LFe(OBz)(Py)}]/[\mathrm{LFe(OBz)}]_0 \qquad (5)$$

$$[\mathrm{LFe(OBz)}]_0 = [\mathrm{LFe(OBz)}] + [\mathrm{LFe(OBz)(Py)}] \qquad (6)$$

Here, δ denotes the chemical shift of the pyrazole 4-position observed in the presence of pyridine (eq 4), while δ_1 and δ_2 are the chemical shift values of pure **4** and the pyridine adduct of **4**, respectively (δ_1 = 63.2, δ_2 = 55.7 ppm). $[\mathrm{LFe(OBz)}]_0$ is the initial concentration of **4** used for the ^{1}H-NMR measurement (eq 6). As expected from eq 3, $1/(\delta - \delta_2)$ was dependent on the concentration of pyridine in a linear relationship (see Figure S1). From the slope, the binding constant *K* was determined to be 13 M^{-1}. Formation constants for metalloporphyrin–pyridine adducts have been explored in detail.[40] The formation constant for **4** is lower than those reported for Zn(TPP) (4800 M^{-1}) and Co(*p*-OMe·TPP) (480 M^{-1}) and comparable to that for Hg(TPP) (15 M^{-1}). It is also considerably lower than that observed for the binding of the first axial base to a ferrous porphyrin (1500 M^{-1}).[41] It is likely that steric effects play an important role in lowering the affinity.

While most σ-donor ligands are easily bound to the five-coordinate complex **4** to form a six-coordinate adduct, the π-acid CO was found not to react with the complex. The IR and ^{1}H-NMR of **4** recorded under 1 atm CO does not show any indication of CO binding to **4**. This is in striking contrast with the high affinity of CO to ferrous porphyrin complexes. It is noteworthy that none of non-heme iron proteins have been reported to form a stable CO adduct, whereas CO binds strongly to the reduced states of heme proteins. The inertness of CO can be understood in terms of ligand field strength where six-coordination in the non-heme systems fails to achieve the low-spin state necessary for good π-back bonding and consequent ligand field stabilization.

Reversible Formation of Dioxygen Adducts. As described above, the carboxylate ferrous complex **4** was found to bind a wide variety of externally added small ligands. This prompted us to explore the reactivities of the carboxylate complexes toward dioxygen. Complex **4** does not exhibit a characteristic absorption band in the visible region as shown in Figure 5. When the solution was treated with 1 atm dioxygen at –50 °C, a striking color change to intense bluish green was noted. The solution exhibits an absorption band at 682 nm with an absorption coefficient of 3450 cm^{-1} M^{-1}/2Fe as shown in Figure 5, which is suggested to be associated with a LMCT transition. The reaction of **4** with dioxygen is very temperature dependent. Thus, at –50 °C, the formation of the oxygenated species is irreversible. In contrast, when the solution was exposed to 1 atm dioxygen at room temperature, the color changed to brown-orange irreversibly (more details are described below). At –20 °C, the binding of dioxygen was found to occur reversibly. At this temperature, when dioxygen was bubbled into a toluene solution of **4**, the characteristic absorption band appeared at 682 nm and disappeared upon bubbling of argon, indicative of the regeneration of **4**. A second treatment with dioxygen reproduced the characteristic band at 682 nm, with an intensity approximately identical to the initial one.[37] Repetitive experiments established that more than 10 cycles of reversible binding of dioxygen are possible with this system at –20 °C in toluene with loss of the dioxygen binding capability of no more than 30%. Exposure of **4** to 1 atm dioxygen at room temperature afforded an irreversible color change to reddish brown (more details later).

With other carboxylate complexes $Fe(OOCR)(HB(3,5\text{-}iPr_2pz)_3)$ (R = Me, Et, C_6H_4-*p*-NH_2, C_6H_4-*p*-Cl, C_6H_4-*p*-NO_2, C_6H_4-*p*-Me), similar bluish green complexes were generated upon exposure to dioxygen at low temperature. However, when a ferrous complex with a more hindered carboxylate was employed, formation of such an adduct did not occur. For instance, $Fe(OOCAd)(HB(3,5\text{-}iPr_2pz)_3)$ (OOCAd denotes 1-adamantylcarboxylate) and $Fe(OOCtBu)(HB(3,5\text{-}iPr_2pz)_3)$ do not react with 1 atm dioxygen neither at –78 °C nor at room temperature. Reaction with dioxygen under reflux conditions in toluene, resulted in the color change of the solution into reddish brown, implying irreversible oxidation to a ferric product, although its structure has not yet been identified. The complex $Fe(OOCiPr)(HB(3,5\text{-}iPr_2pz)_3)$ exhibited unique behavior; a characteristic yellowish green solution was generated upon exposure to 1 atm dioxygen at –78 °C. Because of its instability, however, the characterization of the formed species remains to be completed.

---

(40) Smith, K. M. *Porphyrins and Metalloporphyrins*; Elsevier: Amsterdam, 1975.

(41) Brault, D.; Rougee, M. *Biochemistry* **1974**, *13*, 4591.

Table 3. ^{1}H-NMR Spectral Data of 4 in the Presence of 1 Equiv of Externally Added Ligands[a]

	Pz*H*	*C*HMe$_2$	*C*HMe$_2$	Ph*H*(*o*)	Ph*H*(*m*)	CH*Me*$_2$	Ph*H*(*p*)	CH*Me*$_2$	B*H*
LFeOBz	63.2	13.3	11.7	11.7	9.1	3.7	1.8	-1.5	-9.5
LFeOBz + MeCN	63.2	13.2	11.7	11.7	9.0	3.7	1.9	-1.5	-9.6
LFeOBz + DMF	62.6	12.2	12.2	11.2	8.9	3.2	2.2	-0.7	-11.5
LFeOBz + DMSO	62.5	12.0	13.4	11.0	8.7	2.9	2.2	-0.4	-12.1
LFeOBz + Py	59.9	8.3	16.2	9.1	7.6	2.3	4.0	1.9	-18.4
LFeOBz + PMe$_3$	63.1	13.2	11.6	11.6	9.0	3.6	1.8	-1.5	-9.6
LFeOBz + PPh$_3$	63.2	13.3	11.8	11.8	9.1	3.7	1.9	-1.5	-9.4
LFeOBz + NEt$_3$	63.2	13.3	11.7	11.7	9.1	3.7	1.9	-1.5	-9.4

[a] Benzene-*d*$_6$, 270 MHz, 27 °C.

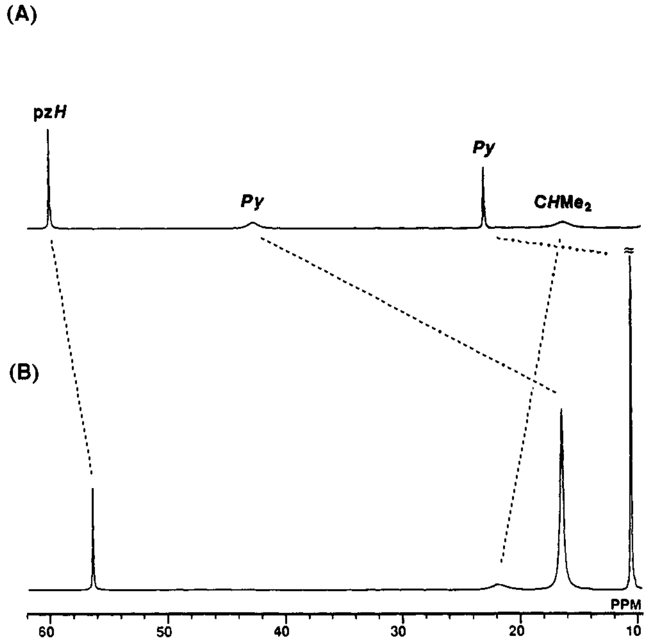

Figure 4. ^{1}H-NMR of 4 in the presence of pyridine recorded at 270 MHz in benzene-*d*$_6$ at 27 °C: (A) Py/4 = 1; (B) Py/4 = 10.

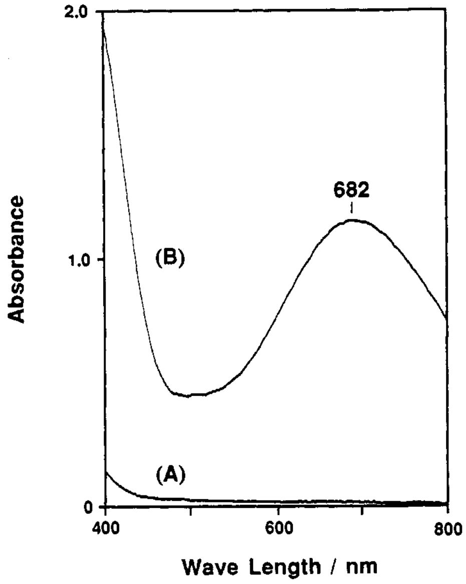

Figure 5. UV-vis spectra of 4 in toluene at -50 °C under argon (A) and dioxygen (B) atmosphere. The concentration of 4 is 0.67 mM.

In order to clarify the structural factors responsible for the inertness of Fe(OOCtBu)(HB(3,5-iPr$_2$pz)$_3$) (**13**) toward dioxygen, the crystal structure of **13** was determined. A perspective view is presented in Figure 6 and the selected structural parameters are summarized in Table 4. As in **2** and **4**, the carboxylate group is bound to the iron in an unsymmetric bidentate coordination mode and the iron is five coordinate. There is, however, a distinctive feature seen in the coordination geometry around the iron. While the iron is five coordinate as in **2**, the geometry is best described as trigonal bipyramidal rather than square pyramidal. The trigonal basal plane consists of two nitrogen atoms from the tris(pyrazolyl)borate ligand and one oxygen atom from the carboxylate, although it is considerably distorted. The other carboxylate oxygen (O2) and N11 serve as apical ligands. Accordingly, the bond distances Fe-O2 and Fe-N11 are distinctly elongated. Comparison of the molecular structures of **2** and **13** indicates that the open coordination space opposite to N31 is very limited in **13** because it is highly shielded with two isopropyl

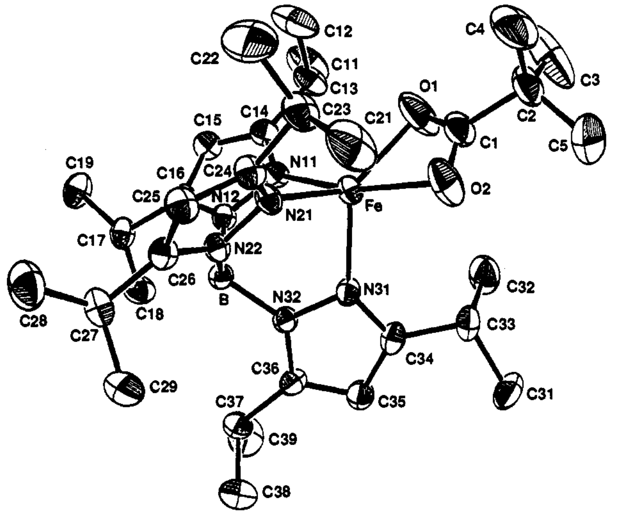

Figure 6. ORTEP view of Fe(OOCtBu)(HB(3,5-iPr$_2$pz)$_3$) (**13**).

Table 4. Selected Bond Distances (Å) and Angles (Deg) for Fe(OOCtBu)(HB(3,5-iPr$_2$pz)$_3$) (**13**)

	Bond Distances		
Fe-O1	2.069(4)	N21-N22	1.376(3)
Fe-O2	2.167(2)	N22-B	1.553(4)
Fe-N11	2.108(2)	N31-N32	1.387(3)
Fe-N21	2.070(2)	N32-B	1.549(4)
Fe-N31	2.069(3)	C1-C2	1.533(5)
O1-C1	1.191(4)	C2-C3	1.474(9)
O2-C1	1.252(6)	C2-C4	1.481(8)
N11-N12	1.372(4)	C2-C5	1.471(7)
N12-B	1.550(4)		
	Bond Angles		
O1-Fe-O2	59.2(1)	N21-N22-B	118.6(2)
O1-Fe-N11	105.2(1)	Fe-N31-N32	116.1(2)
O1-Fe-N21	131.8(1)	N31-N32-B	118.6(2)
O1-Fe-N31	133.3(1)	N12-B-N22	109.1(3)
O2-Fe-N11	164.4(1)	N12-B-N32	109.0(2)
O2-Fe-N21	103.2(1)	N22-B-N32	110.6(2)
O2-Fe-N31	101.8(1)	O1-C1-O2	118.0(4)
N11-Fe-N21	87.10(8)	O1-C1-C2	123.1(4)
N11-Fe-N31	89.29(9)	O2-C1-C2	118.8(3)
N21-Fe-N31	92.3(1)	C1-C2-C3	109.7(3)
Fe-O1-C1	94.5(3)	C1-C2-C4	107.7(3)
Fe-O2-C1	88.1(2)	C1-C2-C5	109.7(4)
Fe-N11-N12	115.2(2)	C3-C2-C4	109.5(6)
N11-N12-B	119.3(2)	C3-C2-C5	109.1(6)
Fe-N21-N22	115.9(2)	C4-C2-C5	111.0(5)

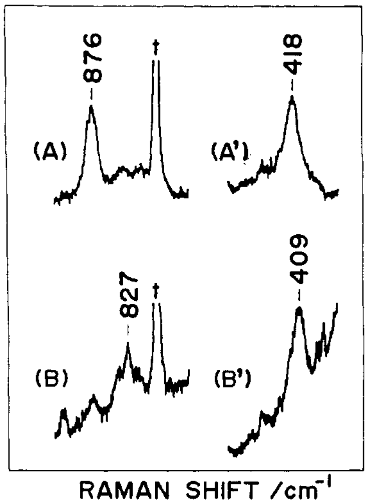

Figure 7. Resonance Raman spectrum of the dioxygen adduct of **4**: (A and A′) $^{16}O_2$ adduct; (B and B′) $^{18}O_2$ adduct; recorded at −80 °C; excitation 676 nm, 20 mW; exposure time 3.2 s; number of scan 100. Peaks marked by a dagger are due to the solvent (toluene).

groups and the bulky carboxylate (see Figure 2 and Figure 6). This presumably accounts for the inertness of **13** toward dioxygen binding.

The energy of a charge transfer band correlates with the electronic property of the metal center and consequently the ligand environment. On the basis of the resonance Raman results (vide infra), we assign the blue-green band at ca. 680 nm to the peroxide-to-iron LMCT band. To test the effect of the carboxylate group on the charge transfer band, the band maxima of the dioxygen adducts of four different carboxylate complexes, Fe(OOCR)-(HB(3,5-iPr$_2$pz)$_3$) (R = Me, C_6H_5, C_6H_4-*p*-NH_2, C_6H_4-*p*-NO_2) were examined in toluene at −50 °C under 1 atm dioxygen. Although accurate determination of the peak position was not easy to accomplish because of the broad shape of the band, it was evident that the adducts have an absorption maximum near 685 nm that does not shift significantly when different carboxylates are used. This may indicate that the electronic state of the Fe_2O_2 chromophore is dominated by the strongly electron donating ligand HB(3,5-iPr$_2$pz)$_3$ and that the contribution of the carboxylate group is not significant.

Resonance Raman Spectrum of the Dioxygen Adduct of Fe(OBz)(HB(3,5-iPr$_2$pz)$_3$) (4). To gain more insight into the structure of the dioxygen adduct, resonance Raman spectra of the oxygenated product of **4** were measured in toluene at −80 °C with excitation at 676 nm. The results are presented in Figure 7, where the spectra of $^{16}O_2$ (A and A′) and $^{18}O_2$ derivatives (B and B′) are displayed. With $^{16}O_2$, two characteristic bands (876 and 418 cm^{-1}) were observed in the frequency regions where the ν(O–O) and ν(Fe–O$_2$) of a transition metal bound peroxide ion are expected, respectively. These bands were shifted to 827 and 409 cm^{-1} with the derivative prepared from $^{18}O_2$ as shown in spectrum B, while a small amount of the concomitant $^{16}O_2$ derivative is present. The magnitudes of the frequency shifts are in reasonable agreement with the values expected from the diatomic harmonic approximations (50 and 15 cm^{-1}, respectively). Accordingly, the 876 and 418 cm^{-1} bands are assigned to the O–O and Fe–O$_2$ stretching vibrations, respectively. No band whose frequency is susceptible to the ^{18}O labeling was observed in the 1000–1200 cm^{-1} region, where ν(O–O) of a superoxide complex is normally observed. Therefore, the possibility that the oxygenated species of **4** is a superoxo complex is excluded. The manometric measurement of the O_2 uptake at −78 °C is ca. 0.5 mol/mol of **4**. These facts led us to conclude that the adduct formed between **4** and dioxygen is a μ-peroxo dinuclear ferric complex. While the formation of such a μ-peroxo species has been suggested in a variety of reactions between ferrous complexes and dioxygen,[34–36] the only credible characterization of such a species is for porphyrin ligand systems where the μ-peroxo species was detected and characterized by ^{1}H-NMR, Mössbauer, and resonance Raman spectroscopy at low temperature.[42–45] The others were not well characterized presumably because of their instability.[34–36]

The Raman bands attributable to the O–O and Fe–O$_2$ stretching were not observed upon blue and green excitation, implying that the 682 nm absorption band arises from a charge transfer transition between the peroxide and iron. The O–O stretching frequency of the dioxygen adduct of **4** is located in a frequency region typical for peroxo transition metal complexes (800–900 cm^{-1}).[46,47] It is slightly higher than that of oxyhemerythrin (845 cm^{-1}), which is a hydroperoxo complex.[48] The Fe–O$_2$ stretching bands of the peroxo complexes are located in the region of 470–500 cm^{-1}.[47] Hence, the frequency observed for the present peroxo complex (418 cm^{-1}) is exceptionally low. This may reflect some structural characteristic of the present μ-peroxo complex, but a more detailed spectroscopic exploration is required to address the origin of this unusual feature. Besides the present work, two μ-peroxo diferric complexes containing a carboxylate ligand have been explored by resonance Raman spectroscopy recently. The ν(O–O) and ν(Fe–O$_2$) reported are 900, 476 cm^{-1} for [Fe$_2$(*N*-Et-HPTB)(O$_2$)(OBz)]$^{2+}$ and 918/891 (Fermi doublet), 486/450 (Fermi doublet) cm^{-1} for [Fe$_2$(6-Me-HPTP)(O$_2$)-(OBz)]$^{2+}$, respectively.[21,22]

^{1}H-NMR of the Dioxygen Adducts of 4. The ^{1}H-NMR spectrum of the dioxygen adduct of **4** is shown in Figure 8A. The signal pattern is very complicated, and the assignment of the spectrum could not be accomplished by simple comparison with that of **4**. This is attributable to the asymmetric structure of the dioxygen adduct as we discuss below on the basis of magnetic properties and EXAFS results. The signals span a narrower range than that observed for **4**. The most down-shifted signal at 34.6 ppm is assignable to the proton at the 4-position of the pyrazole ring. This assignment is supported by the spectrum of the dioxygen adduct of Fe(OBz)(HB(3,5-iPr$_2$-4-Brpz)$_3$) which is presented in Figure 8B, where no signal is observed at 30–35 ppm. Since **4** and the other mononuclear carboxylate complexes, all of which have $S = 2$ ground states, give rise to a signal at ca. 63–65 ppm for the pyrazole 4-proton, the shift to 34.6 ppm indicates that the dioxygen adduct has an effective magnetic moment considerably diminished from that of **4**. This may be accounted for by an antiferromagnetic interaction between the two high-spin ferric centers in the dioxygen adduct mediated by the peroxide ion, lending support to the assignment that the dioxygen adduct is a μ-peroxo dinuclear ferric complex.

Magnetic Susceptibility of the Dioxygen Adduct of 4. Variable temperature magnetic susceptibility data were collected in the range 2–200 K on a microcrystalline precipitate of the dioxygen adduct of **4** isolated and maintained below −70 °C. The effective magnetic moment on a per dimer basis is plotted in Figure 9. The extrapolated room temperature moment of ~4.8 μ_B is considerably lower than the spin-only value for high-spin iron(III) (8.3 μ_B) as consistent with the ^{1}H-NMR results. The data falls off rapidly with decreasing temperature toward diamagnetism. These features are indicative of moderately strong antiferromagnetic

---

(42) (a) Chin, D.-H.; Gaudio, J. D.; La Mar, G. N.; Balch, A. L. *J. Am. Chem. Soc.* **1977**, *99*, 5486. (b) Chin, D.-H.; La Mar, G. N.; Balch, A. L. *J. Am. Chem. Soc.* **1980**, *102*, 4344.

(43) Simonneaux, G.; Scholz, W. F.; Reed, C. A.; Lang, G. *Biochim. Biophys. Acta* **1982**, *714*, 1.

(44) Mizutani, Y.; Hashimoto, S.; Tatsuno, Y.; Kitagawa, T. *J. Am. Chem. Soc.* **1990**, *112*, 6809.

(45) Paeng, I. R.; Nakamoto, K. *J. Am. Chem. Soc.* **1990**, *112*, 3289.

(46) Gulbelmann, M. H.; Williams, A. F. *Struct. Bonding (Berlin)* **1983**, *55*, 1.

(47) Brennan, B. A.; Chen, Q.; Juarez-Garcia, C.; True, A. E.; O'Connor, C. J.; Que, L., Jr. *Inorg. Chem.* **1991**, *30*, 1937.

(48) Kaminaka, S.; Takizawa, H.; Handa, T.; Kihara, H.; Kitagawa, T. *Biochemistry* **1992**, *31*, 6997.

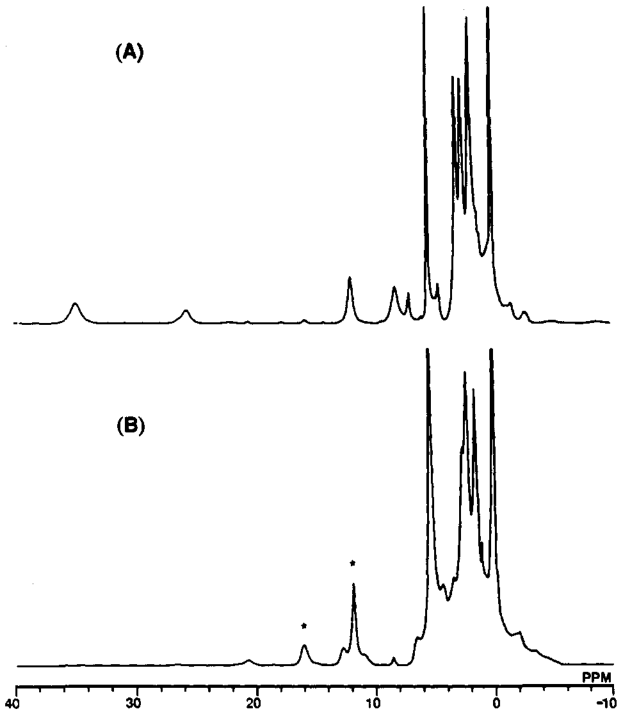

Figure 8. ^{1}H-NMR spectrum of the dioxygen adduct of **4** recorded in CD_2Cl_2: (A) $[Fe(OBz)(HB(3,5\text{-}iPr_2pz)_3)]_2(O_2)$ prepared in situ under 1 atm O_2 at -50 °C; (B) $[Fe(OBz)(HB(3,5\text{-}iPr_2\text{-}4\text{-}Brpz)_3)]_2(O_2)$ generated in situ at -80 °C. Even at this low temperature, the binding of O_2 is incomplete because of low affinity of $Fe(OBz)(HB(3,5\text{-}iPr_2\text{-}4\text{-}Brpz)_3)$ to O_2 and thus signals due to the ferrous complex unreacted are observed (marked with an asterisk).

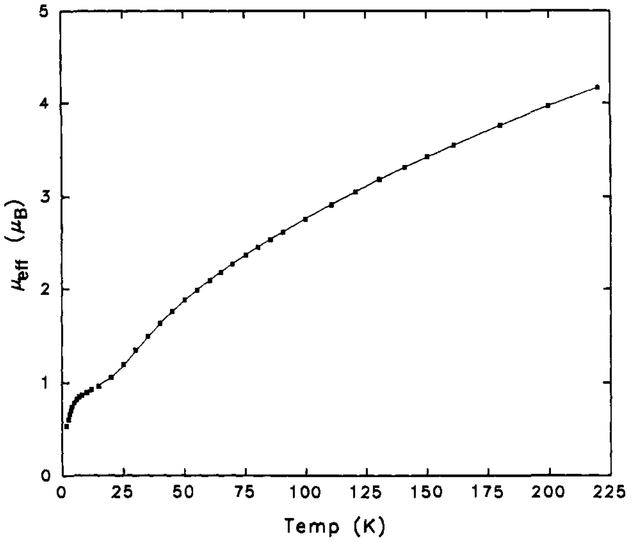

Figure 9. Magnetic moment versus temperature for dioxygen adduct of **4**. The solid line is a theoretical fit with $J = -33$ cm^{-1}, $g = 2.00$, $\Delta\chi_{diam} = +150 \times 10^{-6}$, and 0.87% paramagnetic impurity.

coupling. An excellent fit was obtained for the 20–220 K data using standard spin Hamiltonian treatment of two interacting high-spin iron(III) centers ($H = -2J\cdot S_1\cdot S_2$). The data below 20 K are accounted for by the presence of a 0.87 w % paramagnetic $S = {}^5/_2$ impurity, a chemically reasonable assumption given the thermal instability of the compound. The fit yields $J = -33$ cm^{-1} when g is fixed at 2.00 and χ_{diam} is held to within 15% of the value calculated from Pascal's constants. Data were also collected on the dioxygen adduct of the acetate complex $Fe(OAc)(HB(3,5\text{-}iPr_2pz)_3)$ (**2**). While qualitatively similar, they gave a less satisfactory fit owing to a higher level of impurity.

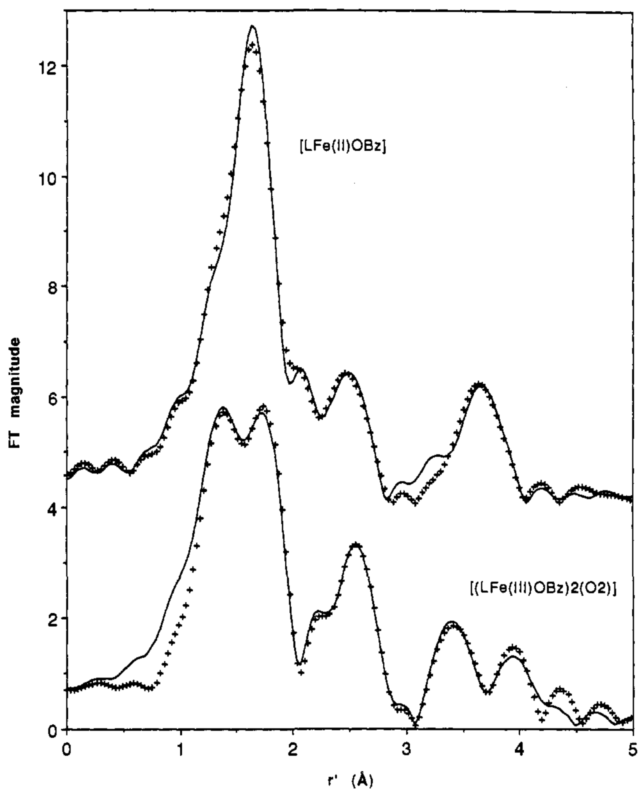

Figure 10. Fourier transforms of EXAFS data (+) and multishell fits (—) of $Fe(OBz)(HB(3,5\text{-}iPr_2pz)_3)$ (**4**) (top) and $[Fe(OBz)(HB(3,5\text{-}iPr_2\text{-}pz)_3)]_2(O_2)$ (bottom).

The good fit obtained for the susceptibility data strongly endorses a dimeric structure. A bridging peroxide ligand is expected to mediate moderately strong antiferromagnetic coupling between high-spin iron(III) atoms although the J value of -33 cm^{-1} is considerably lower in magnitude than those reported in other μ-peroxo dimers (-100 to -70 cm^{-1}).[21b,49] This relatively weak antiferromagnetic property of the μ-peroxo adduct of **4** has structural implications which are discussed below.

EXAFS Analyses of the Dioxygen Adduct. (a) XANES Region. The 1s → 3d transition is a feature of the preedge region of the X-ray absorption spectra of transition metal complexes with partially filled 3d orbitals. Its intensity has been shown to relate to the coordination number of the complex.[50] $Fe(OBz)(HB(3,5\text{-}iPr_2pz)_3)$ (**4**) has a 1s → 3d preedge peak area of 10.7 units, which is consistent with a five-coordinate iron center. The dioxygen adduct, on the other hand, had a 1s → 3d peak area of 4.7 units, which suggests that the iron centers in the complex have become six-coordinate upon exposure to dioxygen, the dioxygen ligand occupying the vacant site in the precursor complex.

(b) EXAFS Studies. X-ray absorption spectra were collected for both **4** and its crystallographically characterized acetonitrile adduct **3**. The unsolvated complex $Fe(OBz)(HB(3,5\text{-}iPr_2pz)_3)$ (**4**) was the precursor complex of choice for analysis, because the acetonitrile adduct **3** exhibited spectra that varied in each of the four samples studied, probably due to some acetonitrile loss. Our EXAFS analysis of **4** agrees well with the X-ray structure of the unsolvated acetate complex **2**.

Figure 10 compares the Fourier transforms of the EXAFS data of **4** and its dioxygen adduct. Principal features of the precursor complex include a large peak at $r' = 1.6$ Å with a

---

(49) Balch, A. L.; Chan, Y.-W.; Cheng, R.-J.; La Mar, G. N.; Latos-Grazynski, L.; Renner, M. W. *J. Am. Chem. Soc.* **1984**, *106*, 7779.

(50) (a) Roe, A. L.; Schneider, D. J.; Mayer, R. J.; Pyrz, J. W.; Que, L., Jr. *J. Am. Chem. Soc.* **1984**, *106*, 1676. (b) Randall, C. R.; Zang, Y.; True, A. E.; Que, L., Jr.; Charnock, J. M.; Garner, C. D.; Fujishima, Y.; Schofield, C. J.; Baldwin, J. E. *Biochemistry* **1993**, *32*, 6664.

Table 5. Restricted Multishell Fits of the EXAFS data of [LFe(OBz)] and Its Dioxygen Adduct[a]

fit	back transform range (Å)	*n*	Fe–O[b]	σ^2	*n*	Fe–N/O	σ^2	*n*	Fe–C/O	σ^2	*n*	Fe–Fe	σ^2	R_{FF}[c]
[LFe(OBz)]	1st coord sphere													
1	0.9–2.4				4	2.09	0.0038							0.21
2	0.9–2.4				4	2.09	0.0038	1	2.47	0.0012				0.11
[{LFe(OBz)}$_2$(O$_2$)]														
sample no. 1	1st coord. sphere													
3	1.0–2.3				6	2.08	0.0159							0.34
4	1.0–2.3	1	1.89	0.0010	5	2.12	0.0075							0.17
5	1.0–2.3	1	1.90	0.0018	5	2.12	0.0082	1	2.52	0.0049				0.06
sample no. 1	multishell fits													
6	0.8–4.2	1	1.90	0.0021	5	2.12	0.0084	1	2.52	0.0045	1	4.33	0.0075	0.09
sample no. 2														
7	0.8–4.2	1	1.91	0.0050	5	2.13	0.0078	1	2.53	0.0054	1	4.36	0.0065	0.11

[a] Complete multishell fits are in Table S1. [b] Distances are in Å and Debye–Waller factors (σ^2) are in Å^2. [c] R_{FF} is the residual, RMS$_{dev}$/RMS$_{dat}$, of the Fourier-filtered data.

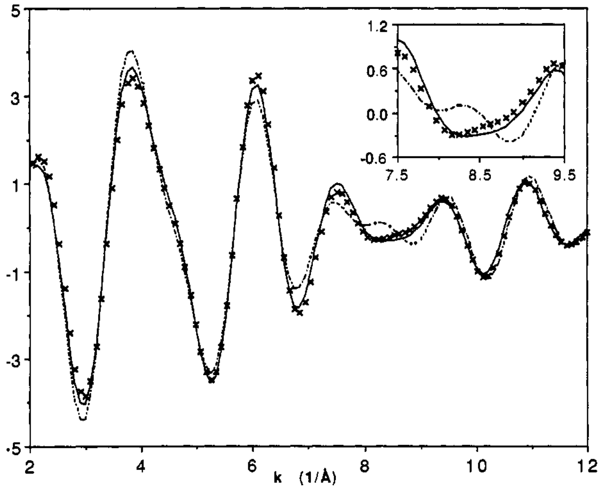

Figure 11. Fourier-filtered (range = 0.8–3.0 Å) back transformed data (×) and multishell fits with an Fe–C/O interaction at r' = 2.5Å (—) and without such an interaction (---).

shoulder at 2.1 Å, corresponding to the first coordination sphere, and smaller peaks at 2.5 and 3.6 Å. Upon exposure to dioxygen, the r' = 1.6 Å feature splits into two peaks and a new feature at r' = 3.9 Å appears. Other changes include an increase in the intensity of the feature at r' = 2.5 Å and a shift of the feature at r' = 3.6 to 3.4 Å.

The first coordination sphere of **4** can be modeled well with four Fe–N/O at 2.09 Å and one Fe–C/O at 2.47 Å. These distances correspond to those found in the crystal structure of Fe(OAc)(HB(3,5-iPr$_2$pz)$_3$) (**2**) which shows an average Fe–N/O distance of 2.08 Å for the three pyrazole nitrogens and one carboxylate oxygen and an Fe–C distance of 2.48 Å for the carbon atom of the chelated carboxylate ligand. The 2.23 Å distance corresponding to the more distant carboxylate oxygen does not appear to contribute significantly to the EXAFS data. In the EXAFS analysis (Table 5), the one-shell fit was not affected by the addition of another scatterer at 2.2–2.3 Å, but was improved only by the inclusion of the Fe–C/O interaction at 2.47 Å. Thus, there is a good match between the distances derived from the EXAFS fit and those found in the crystal structure. However, the cooordination number required by the EXAFS fit is one less than that indicated by the XANES data. This may arise because of the lack of correlation between the motions of the iron atom and ligand atoms.[50]

The outer shells of the starting material represented by the somewhat broad peaks at r' = 2.5 and 3.6 Å in the Fourier transform of the data (Figure 10) can be simulated with 2.3 nitrogen atoms at 3.0 Å (from its crystal structure, the acetate complex has three nitrogen atoms at an average distance of 2.95 Å from the iron center, and no tris(pyrazolyl)borate carbon atoms less than 3.2 Å away), 2.7 carbon atoms at 3.6 Å, and 3 carbon atoms at 4.1 Å. In addition, the model was refined by the addition of a shell of 5.4 carbon atoms at 4.26 Å. This combination is but one approach to model the large range of Fe–C/N distances present in the complex. The shell at 3.6 Å had a large Debye–Waller factor, suggesting a large range of distances for the atoms comprising the shell. It is likely then that this shell is compromised by choosing groups of distances for iron–carbon interactions that afford the best overall fit for the data.

Very similar fits were obtained for both samples of the dioxygen adduct of **4** in toluene solution (Table 5). One-shell fits were significantly improved by the inclusion of a short Fe–O interaction at ca. 1.9 Å and a long Fe–C interaction at ca. 2.5 Å. The best fit for each data set had one Fe–O at 1.90–1.91 Å, five Fe–N/O interactions at 2.12–2.13 Å, and one Fe–C at 2.52–2.53 Å.

The splitting of the largest feature in the Fourier transform of the EXAFS data into two peaks justifies the inclusion of the short Fe–O distance in the fit (Figure 10). This new feature most likely derives from the coordination of the μ-peroxo group. For comparison, the Fe–O bond in the O$_2$ adduct of the picket fence porphyrin[51] is 1.898(7) Å. In μ-1,2-peroxo-bridged dinuclear complexes, the M–O band distances are 1.893(15) and 1.863(17) Å for [Co$_2$(BPMP)(OBz)O$_2$](BF$_4$)$_2$,[52] 1.852(5) Å for [{Cu(TMPA)}$_2$O$_2$](PF$_6$)$_2$),[53] and 1.83(2) Å for [(Me$_3$TACN)$_2$Mn$_2$(O)$_2$O$_2$](ClO$_4$)$_2$;[54] however, these complexes contain metal centers with smaller ionic radii. The only crystallographically characterized ferric peroxide complex is [Fe$_6$O$_2$(OH)$_2$(OBz)$_1$$_{32}$(H$_2$O)(1,4-dioxane)], which contains a μ_4-peroxo moiety with an average Fe–O$_{peroxo}$ bond distance of 2.01 Å.[55] The 1.90 Å scatterer in the dioxygen adduct is thus reasonably assigned to the peroxo ligand. This compares to 1.80 Å deduced from EXAFS studies on [Fe(O$_2$)(TPP)]$^-$.[56]

The shell of five Fe–N/O interactions at 2.12–2.13 Å is at a distance expected for aromatic nitrogen (2.1–2.2 Å)[57,58] and chelated carboxylate ligands (2.0–2.3 Å),[59] although the Debye–Waller factor of 0.008 Å^2 suggests that there is a range of distances for the atoms comprising this shell. The average Fe–N/O distance in the dioxygen adduct is similar to that found for the starting

---

(51) (a) Collman, J. P.; Gagne, R. R.; Reed, C. A.; Halbert, T. R.; Lang, G.; Robinson, W. T. *J. Am. Chem. Soc.* **1975**, *97*, 1427. (b) Jameson, G. B.; Molinaro, F. S.; Ibers, J. A.; Collman, J. P.; Brauman, J. I.; Rose, E.; Suslick, K. S. *J. Am. Chem. Soc.* **1980**, *102*, 3224.

(52) Suzuki, M.; Ueda, I.; Kanatomi, H.; Murase, I. *Chem. Lett.* **1983**, 185.

(53) Jacobson, R. R.; Tyeklar, Z.; Farooq, A.; Karlin, K. D.; Liu, S.; Zubieta, J. *J. Am. Chem. Soc.* **1988**, *110*, 3690.

(54) Bossek, U.; Weyhermüller, T.; Wieghardt, K.; Nuber, B.; Weis, J. *J. Am. Chem. Soc.* **1990**, *112*, 6387.

(55) Micklitz, W.; Bott, S. G.; Bentsen, J. G.; Lippard, S. J. *J. Am. Chem. Soc.* **1989**, *111*, 372.

(56) Friant, P.; Goulon, J.; Fischer, J.; Ricard, L.; Schappacher, M.; Weiss, R.; Momenteau, M. *Nouv. J. Chim.* **1985**, *9*, 33.

(57) Armstrong, W. H.; Lippard, S. T. *J. Am. Chem. Soc.* **1984**, *106*, 4632.

(58) Armstrong, W. H.; Spool, A.; Papaefthymiou, G. C.; Frankel, R. B.; Lippard, S. J. *J. Am. Chem. Soc.* **1984**, *106*, 3653.

(59) Poganiuch, P.; Liu, S.; Papaefthymiou, G. C.; Lippard, S. J. *J. Am. Chem. Soc.* **1991**, *113*, 4645.

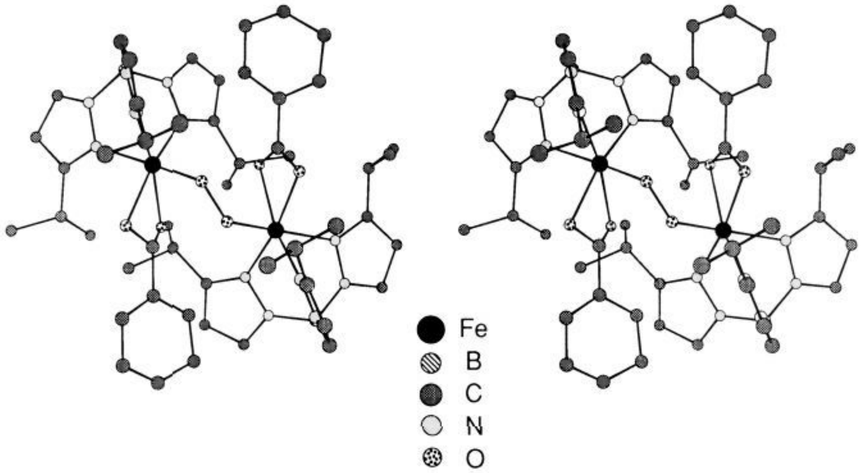

Figure 12. Stereorepresentation of the proposed structure for $[Fe(OBz)(HB(3,5\text{-}iPr_2pz)_3)]_2(O_2)$ with ∠Fe–O–O = 127.5°, ∠Fe–O–O–Fe = 90°, and r_{Fe-Fe} = 4.33 Å; produced using Chem3D Plus and parameters from the crystal structure of $Fe(OBz)(MeCN)(HB(3,5\text{-}iPr_2pz)_3)$. The 5-iPr carbons and all hydrogen atoms have been omitted for clarity.

material, indicating that the iron–ligand distances are not greatly perturbed by dioxygen binding despite the redox change at the iron center.

The inclusion of the Fe–C interaction at ~2.5 Å in the first coordination sphere is necessary for a satisfactory fit (Table 5). Specifically, the trough between 7.5 and 9.5 $Å^{-1}$ in the Fourier-filtered (from $r' = 0.8$–3.0 Å) back transform of the data cannot be adequately modeled without a low-Z scatterer at 2.52–2.53 Å (Figure 11, inset). Such a distance is quite reasonable for the carboxylate carbon of a chelated carboxylate ligand, as seen in the structures of $Fe(OAc)(HB(3,5\text{-}iPr_2pz)_3)$ (**2**), $Fe(OBz)(MeCN)(HB(3,5\text{-}iPr_2pz)_3)$ (**3**), and $[Fe_3O(OAc)_6(TACN)]$.[59] While it is also possible that the 2.5 Å distance corresponds to the more distant oxygen of an asymmetrically chelated carboxylate, the presence of a chelated carboxylate in the starting material suggests that it is retained in the dioxygen adduct.

The $r' = 2.5$ Å feature in the Fourier transform of the dioxygen adduct is more intense relative to its precursor. This may be an effect of the more distant oxygen atom of the μ-peroxo group. Given an Fe–O distance of 1.90 Å determined from the EXAFS analysis, a typical O–O distnace of 1.47 Å for a peroxo group, and a typical Fe–O–O angle of 125–130° (from crystallographically characterized dioxygen adducts of ferrous iron complexes),[51,60] the farther oxygen atom would be at 3.0 Å and thus be expected to contribute to the $r' = 2.5$ Å peak in the Fourier transform. Indeed the numbers of scatterers for the precursor complex and the dioxygen adduct differ by about one atom in the shells at 3.0–3.1 Å.

The outer coordination sphere of the dioxygen adduct can be modeled similarly to that of the precursor with various shells of low-Z scatterers. The most interesting feature is the new peak at $r' = 3.9$ Å. Since it is not found in the starting material, it is likely to be a consequence of adduct formation, perhaps resulting from an Fe–Fe interaction. While it was possible to fit this peak with 4–6 carbon atoms at 4.4 Å and either several carbons or one iron at 3.9–4.0 Å (Table S1), the best fits were those with carbon atoms at 4.0 Å and iron at ca. 4.33 Å (Table 5).

Having an Fe–Fe interaction at 4.3–4.4 Å has implications on the structure of the dioxygen adduct. Given the above mentioned considerations for r_{Fe-O}, r_{O-O}, and ∠Fe–O–O, an Fe–O–O–Fe dihedral angle of 180° would give rise to an Fe–Fe separation of 4.8 Å, while an Fe–O–O–Fe dihedral angle of 0° corresponds to an Fe–Fe distance of 3.9 Å. Although the latter distance is consistent with some of the fitting results (Table S1), a dihedral angle of 0° can be ruled out due to the steric bulk of the ligands. Indeed steric repulsions would be minimal with a 180° dihedral angle, but the EXAFS analysis affords an Fe–Fe distance of 4.3 Å, corresponding to a dihedral angle closer to 90°.

Support for such a structure can be obtained from the magnetic properties of the adduct. Both magnetic susceptibility and NMR measurements indicate a diferric complex with relatively weak antiferromagnetic coupling. Studies of other peroxide complexes indicate that the μ-1,2-peroxo unit is an efficient conduit for antiferromagnetic coupling. $[\{Cu(TMPA)\}_2(O_2)](PF_6)_2$[53] and $[Cu(HB(3,5\text{-}iPr_2pz)_3)]_2(O_2)$[61] have an M–O–O–M dihedral angle of 180° and are essentially diamagnetic at room temperature. $\{Fe(TPP)\}_2(O_2)$[49] and $[Fe_2(HPTB)(O_2)](NO_3)_3$[47] are estimated to have *J* values of −100 and −70 cm^{-1}, respectively, from NMR measurements. The former is expected to have a dihedral angle of 180° on steric grounds, while the latter would have a dihedral angle between 0° and 50° on the basis of the structures of multiply bridged peroxide complexes such as $[(Me_3TACN)_2Mn_2(O)_2(O_2)](ClO_4)_2$[54] and $[Co_2(BPMP)(OBz)(O_2)](BF_4)_2$.[52] The weaker coupling observed for the dioxygen adduct of **4** suggests that the peroxide moiety in this adduct is less efficient at mediating the antiferromagnetic interaction. In conjunction with MO calculations (see below), it is suggested that the antiferromagnetic coupling is most efficient when the Fe–O–O–Fe unit has a dihedral angle of 0° or 180° and least efficient for a dihedral angle close to 90°. The combination of the EXAFS analysis with the magnetic properties of the adduct indicates a structure for $[Fe(OBz)(HB(3,5\text{-}iPr_2pz)_3)]_2(O_2)$ with a dihedral angle near 90°. Figure 12 shows how such a dihedral angle can still accommodate the steric bulk of the tris(pyrazolyl)borate ligands, although it is unclear why the adduct prefers such a conformation.

Molecular Orbital Analysis of the μ-Peroxo Adduct. The electronic structure of the μ-peroxo diferric complexes has been examined by the extended Hückel method, focusing mainly on the correlation between the Fe–O–O–Fe skeletal geometry and the magnetic interaction between the ferric centers. In order to avoid complications arising from steric influence, we first explored the simple hydride model, $(H_5Fe)_2(O_2)$, where the idealized octahedral geometry was assumed at each iron site. Our theoretical analysis for $(H_5Fe)_2(O_2)^{6-}$ is analogous to that for a model porphyrin complex, $[(NH_2)_4Fe]_2(O_2)^{4-}$, that was reported earlier by one of us.[62]

The orbital analysis of $(H_5Fe)_2(O_2)^{6-}$ begins with the linear Fe–O–O–Fe structure. Its d-block orbitals are drawn in Figure

---

(60) Holmes, M. A.; Trong, I. L.; Turley, S.; Sieker, L. C.; Stenkamp, R. E. *J. Mol. Biol.* **1991**, *218*, 583.

(61) Kitajima, N.; Fujisawa, K.; Fujimoto, C.; Moro-oka, Y.; Hashimoto, S.; Kitagawa, T.; Toriumi, K.; Tatsumi, K.; Nakamura, A. *J. Am. Chem. Soc.* **1992**, *114*, 1277.

(62) Tatsumi, K.; Hoffmann, R. *J. Am. Chem. Soc.* **1981**, *103*, 3328.

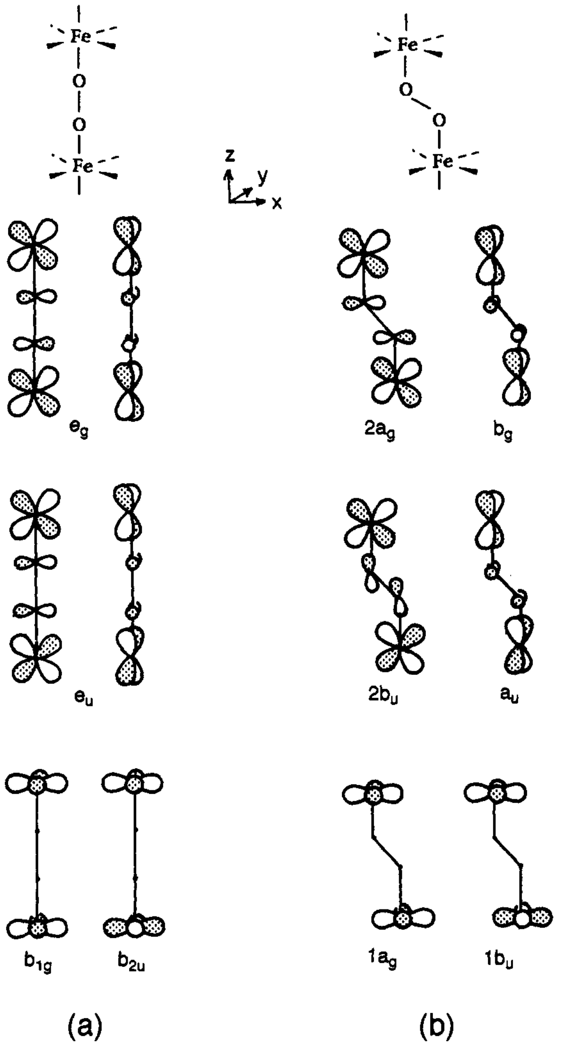

Figure 13. d-Block orbitals of $(H_5Fe)_2(O_2)^{6-}$: (a) with a linear Fe–O–O–Fe spine and (b) with a trans-bent Fe–O–O–Fe spine (Θ = 120°).

13a. The in-phase (b_{1g}) and out-of-phase (b_{2u}) combinations of the Fe $x^2 - y^2$ orbitals are placed at the lower end, since they do not interact with any of the ligand orbitals. Above these orbitals there are two degenerate sets of antibonding combinations of O_2 and Fe dπ orbitals, where the $O_2\pi^*$-(xz,yz) set, e_g, is higher in energy than the $O_2\pi$-(xz,yz) set, e_u. The four higher-lying molecular orbitals associated with Fe xy and Fe z^2 are omitted in the figure. There are 10 electrons in these d-block orbitals, and the e_g orbitals are half-filled. Electron transfer to the $O_2\pi^*$ is extensive, and one may think of this system as two d^5 Fe centers bridged by peroxide. Thus the electron count is appropriate to a model for μ-peroxo diferric complexes.

The left side of Figure 14 shows the Walsh diagram for the simultaneous bending of the two Fe–O–O bonds, as a function of Θ. The trans bending of the Fe–O–O–Fe spine splits both e_g and e_u. The $2a_g$ orbital, which is derived from e_g, is stabilized by diminution of the O–O antibonding interaction, while stabilization of th e_u-derived $2b_u$ orbital is mainly due to relief of the Fe dπ–Oπ repulsive interaction. The other orbital levels are not affected much by the trans bending. We depict in Figure 13b the d-block orbitals at Θ ≈ 127.5°. As a result of the level splitting, b_g and $2a_g$ become the LUMO and the HOMO, respectively, where the HOMO–LUMO gap increases with decrease of Θ.Figure 14 also plots the change in the total energy assuming a low-spin state, which demonstrates that the trans-bent geometry with Θ = 127.5° is favored over the linear form by 0.485 eV.

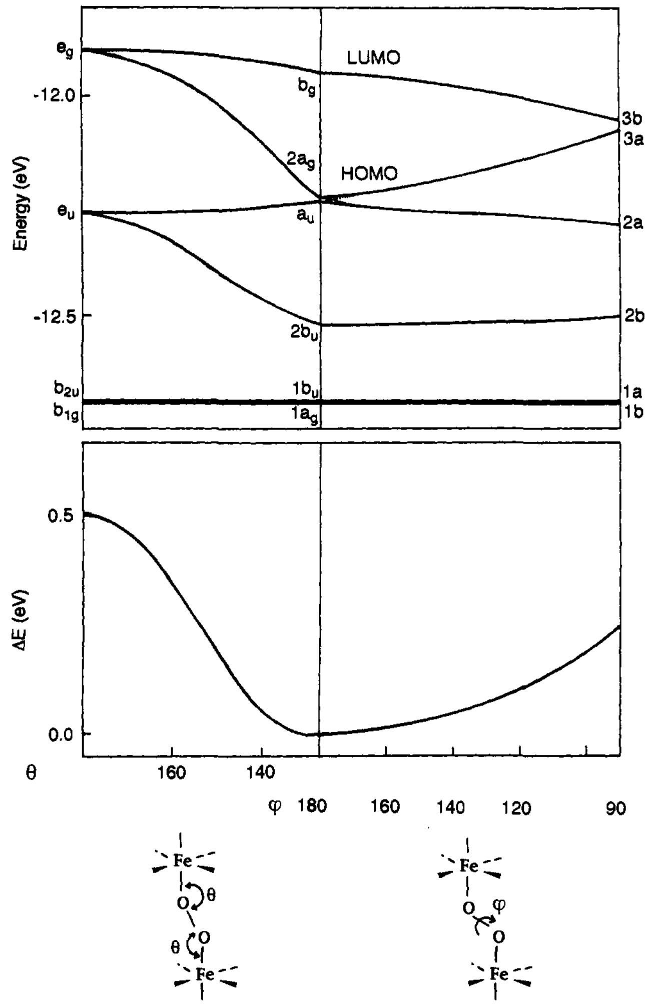

Figure 14. Walsh diagrams and potential energy curves for Fe–O–O–Fe trans bending (left) and twist deformation (right) of $(H_5Fe)_2(O_2)^{6-}$.

We then varied the Fe–O–O–Fe dihedral angle φ from 180° to 90° with the Fe–O–O angles being kept at 127.5°. The Walsh diagram and the total energy curve are given at the right side of Figure 14. An important consequence of this deformation is stabilization of 3b and concomitant destabilization of 3a, which narrows the HOMO–LUMO gap. Because the twisting motion lowers the molecular symmetry from C_{2h} to C_2, the $2a_g$ and a_u orbitals of the trans-bent structure could mix with each other in 2a and 3a. However, the close inspection of their orbital shapes indicates that 3a correlates with a_u and 2a with $2a_g$. Thus, the reason behind the small but notable destabilization of the a_u–3a level is trace to the disruption of the O–Oπ bonding, and the stabilization of the b_g–3b level arises from a decrease of the O–Oπ^* antibonding interaction. The net balance of these opposing effects is that destabilizing of a_u–3a dominates slightly and the twist motion energy is moderate (0.249 eV). As we optimized the Fe–O–O angle Θ = 137.5°. The slight increase of Θ from 127.5° to 137.5° lowers the total energy by 0.048eV probably due to the easing of steric repulsions between the FeH_5 units. It should be noted that hydrogen peroxide slightly favors the twist geometry over the other conformations[63] and that the model porphyrin system, $[(NH_2)_4Fe]_2(O_2)^{4-}$, exhibits a very flat potential surface in the range φ = 180–110°.[62] Interestingly, both planar (φ = 180°) and slightly nonplanar (φ = 166°) structures were found in the same crystal of $K_5[Co(CN)_5]_2(O_2)$.[64]

---

(63) (a) Hunt, R. H.; Leacock, R. A.; Peters, C. W.; Hecht, K. T. *J. Chem. Phys.* **1965**, *42*, 1931. (b) Hunt, R. H.; Leacock, R. A. *J. Chem. Phys.* **1966**, *45*, 3141.

(64) Wang, B. C.; Schaefer, W. P. *Science (Washington D.C.)* **1969**, *166*, 1404.

Table 6. HOMO–LUMO Gaps, Relative Total Energies, and Fe–Fe Distances for the Three Limiting Structures of $(H_5Fe)_2(O_2)^{6-}$ and $[(NH_3)_3(HCO_2)Fe]_2(O_2)^{2+}$

	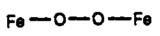	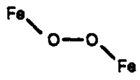	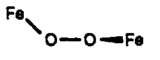
	$(H_5Fe)_2(O_2)^{6-}$		
HOMO–LUMO (eV)	0.0	0.288	0.019
ΔE (eV)	0.0	−0.485	−0.283
Fe-Fe (Å)	5.05	4.628	4.45 (θ = 137.5°)
	$[(NH_3)_3(HCO_2)Fe]_2(O_2)^{2+}$		
HOMO–LUMO (eV)	0.047	0.180	0.041
ΔE (eV)	0.0	−0.429	−0.239
Fe-Fe (Å)	5.05	4.628	4.515 (θ = 140.0°)

Scheme 1

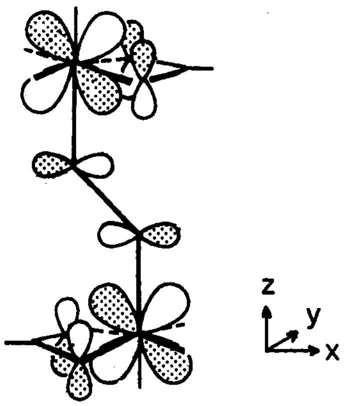

Our next objective was to move from $(H_5Fe)_2(O_2)^{6-}$ to a more realistic μ-peroxo model. To this end we examined the electronic properties of $[(NH_3)_3(HCO_2)Fe]_2^{2+}$, where *fac*-$(NH_3)_3^{1+}$ mimics the tridentate $HB(3,5\text{-}iPr_2pz)_3$ ligand. The essence of our orbital considerations for $(H_5Fe)_2(O_2)^{6-}$ carries over to the more complicated system. For instance, the HOMO–LUMO gap becomes larger as the Fe–O–O bonds are bent from Θ = 180° to 127.5°, and the twist distortion of the trans-bent geometry narrows the HOMO–LUMO gap. Optimization with a twist geometry of φ = 90° again resulted in increase of the Fe–O–O angle to Θ = 140°. Table 6 summarizes the HOMO–LUMO gaps, relative total energies, and Fe···Fe distance calculated for the three limiting geometries of the two model complexes. In going from $(H_5Fe)_2(O_2)^{6-}$ to $[(NH_3)_3(HCO_2)Fe]_2(O_2)^{2+}$, the HOMO–LUMO gap of the trans-bent structure (Θ = 127.5°, φ = 180°) decreases by 0.108 eV. Coordination of the carboxylate ligand brings about repulsive interactions between the Fe *xy* and the asymmetric combination of formate π orbitals, causing destabilization of the "$2a_g$" orbital (HOMO), which in turn gives rise to a smaller HOMO–LUMO gap for $[(NH_3)_3(HCO_2)Fe]_2(O_2)^{2+}$. This orbital interaction is drawn below in Scheme 1. The "b_g" orbital (LUMO) is also destabilized by repulsive interactions between Fe *yz* and the antisymmetric combination of formate π orbitals, but to a lesser extent. Thus, the HOMO–LUMO gap may vary subtly depending on the auxiliary ligands at iron.

From the theoretical analysis of the model μ-peroxo differic complexes, we find three factors that may narrow the HOMO–LUMO gap including (1) increase of the Fe–O–O angle, (2) a twist deformation of the Fe–O–O–Fe skeleton, and (3) the coordination of a carboxylate ligand at iron. Provided that the magnitude of the $-J$ values is controlled values is controlled primarily by the HOMO–LUMO gap, either of the above three factors can account for the weak antiferromagnetic coupling observed for the dioxygen adduct of $Fe(OBz)(HB(3,5\text{-}iPr_2pz)_3)$ (**4**). It is not an easy task to conclude from the theoretical calculations alone which of these factors is responsible for the small $-J$ value. However, the twist deformation (factor 2) seems to be a reasonable candidate according to the EXAFS study, and the relatively flat potential energy curve for the twist motion is not inconsistent with this proposition.

Table 7. Selected Bond Distances (Å) and Angles (Deg) for $(HB(3,5\text{-}iPr_2pz)_3)Fe(OBz)_2(OH)Fe(O)(OBz)_2Fe(HB(3,5\text{-}iPr_2pz)_3)\cdot 6C_7H_8$ (**16·6C₇H₈**)

	Bond Distances		
Fe1–Fe2	3.3811(3)	Fe2–N11	2.21(1)
Fe1–O1	2.02(1)	Fe2–N21	2.20(1)
Fe1–O3	2.07(1)	Fe2–N31	2.25(1)
Fe1–O5	1.92(1)	O1–C41	1.26(2)
Fe2–Fe2′	6.516(5)	O2–C41	1.25(2)
Fe2–O2	2.06(1)	O3–C51	1.20(2)
Fe2–O4	2.05(1)	O4–C51	1.30(2)
Fe2–O5	1.89(1)		
	Bond Angles		
Fe2—Fe1—Fe2′	148.9(2)	O4–Fe2–N11	165.7(5)
O1–Fe1–O1′	168.8(8)	O4–Fe2–N21	86.5(5)
O1–Fe1–O3	88.4(5)	O4–Fe2–N31	82.5(5)
O1–Fe1–O3′	82.8(5)	O5–Fe2–N11	99.4(5)
O1–Fe1–O5	91.3(5)	O5–Fe2–N21	95.7(5)
O1–Fe1–O5′	95.8(5)	O5–Fe2–N31	174.6(5)
O3–Fe1–O3′	75.7(7)	N11–Fe2–N21	84.9(5)
O3–Fe1–O5	91.8(4)	N11–Fe2–N31	85.7(5)
O3–Fe1–O5′	166.3(5)	N21–Fe2–N31	86.7(5)
O5–Fe1–O5′	101.1(6)	Fe1–O1–C41	133(1)
O2–Fe2–O4	97.1(4)	Fe2–O2–C41	134(1)
O2–Fe2–O5	92.0(5)	Fe1–O3–C51	129(1)
O2–Fe2–N11	89.9(5)	Fe2–O4–C51	125(1)
O2–Fe2–N21	171.3(5)	Fe1–O5–Fe2	125.0(6)
O2–Fe2–N31	86.0(5)	O1–C41–O2	125(2)
O4–Fe2–O5	92.8(5)	O3–C51–O4	128(2)

Irreversible Formation of a Trinuclear Ferric Complex from the Dioxygen Adduct. The dioxygen adduct of **4** is reasonably stable at −78 °C but decomposes slowly at −20 °C. Thus, when a toluene solution of the blue-green dioxygen adduct of **4** was allowed to stand at −20 °C under 1 atm dioxygen overnight, the color of the solution turned to reddish brown. From the solution, greenish brown colored crystals (**16**) were obtained in low yield (< 20%). The electronic spectrum of **16** exhibited an intense absorption band at 375 nm (ϵ, 16 400 $M^{-1}\,cm^{-1}$) with two shoulder bands at ca. 490 and 615 nm. A sharp IR band at 3632 cm^{-1} indicates the presence of a hydroxo group. These spectral features are very similar to those of the trinuclear ferric complex $(HB(3,5\text{-}iPr_2pz)_3)Fe(OH)(OAc)_2Fe(O)(OAc)_2Fe(HB(3,5\text{-}iPr_2pz)_3)$ (**17**),[65] implying that **16** adopts a similar trinuclear structural motif. The acetate trimer **17** is readily formed upon exposure of a five-coordinate ferrous complex $Fe(acac)(HB(3,5\text{-}iPr_2pz)_3)$ to dioxygen. This product is apparently a thermodynamic sink in the oxidative degradation of the ferrous complex. As we reported previously, its unusual trinuclear structure containing a (μ-oxo)bis(μ-acetato) and a (μ-hydroxo)bis(μ-acetato) bridge was unambiguously identified from X-ray analysis in conjunction with Mössbauer and magnetic susceptibility studies.[65] The close resemblance of **16** to **17** in its magnetic property and Mössbauer spectrum (see the Experimental Section) suggests strongly that **16** has a trinuclear ferric chromophore containing the (μ-oxo)(μ-hydroxo) unsymmetric bridging unit as in **17**. The X-ray analysis of **16** finally comfirmed the trinuclear structure, although the refinement is not excellent owing to the high disorder of the solvent molecules of crystallization. Figure 15 presents a perspective view of **16**. The bond distances and angles are summarized in Table 7. The acetate trimer **17** sits on a crystallographically imposed center of symmetry, requiring the Fe–Fe–Fe frame to be linear. On the contrary, the central iron in **16** sits on a crystallographically imposed C_2 axis. Accordingly,

---

(65) Kitajima, N.; Amagai, H.; Tamura, N.; Ito, M.; Moro-oka, Y.; Heerwegh, K.; Penicaud, A.; Mathur, R.; Reed, C. A.; Boyd, P. D. W. *Inorg. Chem.* **1993**, *32*, 3583.

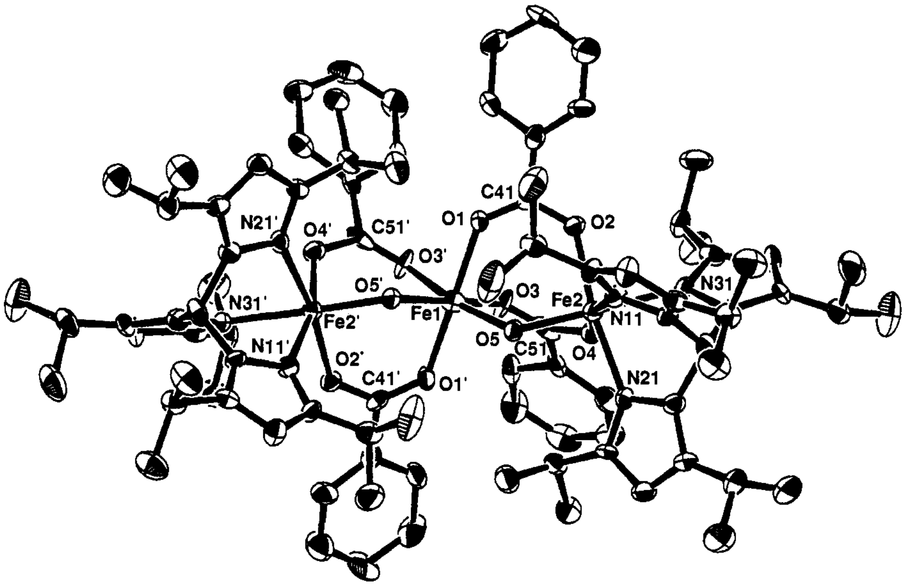

Figure 15. ORTEP view of $(HB(3,5\text{-}iPr_2pz)_3)Fe(OBz)_2(OH)Fe(O)(OBz)_2Fe(HB(3,5\text{-}iPr_2pz)_3)$ (**16**).

the Fe–Fe–Fe frame is bent with the mean angle of 149°. The structural difference is probably due to greater steric hindrance of the benzoate relative to that of the acetate. With the bent structure adopted in **16**, the repulsion between the benzoate groups is minimized more effectively than in the acetate trimer **17**. Despite the crystallographically symmetric structure of **16**, its magnetic and Mössbauer properties are consistent only with an unsymmetric ferric trimer structure having strong antiferromagnetic coupling with an overall $S = {}^5/_2$ ground state. The overall net charge of the complex is neutral on the basis of the crystal structure and the analytical data. Hence, the structure is only consistent with an unsymmetric (μ-oxo)bis(μ-benzoato) and (μ-hydroxo)bis(μ-benzoato) bridges, which cannot be differentiated crystallographically because of serious disorder as observed for **17**.

Summary and Concluding Remarks

In the present study, by using a hindered tris(pyrazolyl)borate ligand, a series of monomeric carboxylate ferrous complexes $Fe(OOCR)(HB(3,5\text{-}iPr_2pz)_3)$ has been synthesized. The ferrous ion is five-coordinate with a N_3O_2 ligand donor set, retaining a structural similarity at least in part to the iron site of non-heme iron proteins which interact with dioxygen. A variety of σ-donating small ligands can bind to the open coordination site to give six-coordinate adducts. The interaction is dominated by ligand-to-metal σ-donating interactions with insignificant π-back bonding interactions. Accordingly, π-acids, such as CO do not bind to the complex. In order to uncover the geometric and electronic factors responsible for the dioxygen binding and activation in proteins such as hemerythrin, Fe-SOD, and lipoxygenase, the reaction between the complexes and dioxygen has been examined. The reactivity of the carboxylate complexes is dramatically dependent on the steric bulk of the carboxylate group. Accordingly, the *tert*-butyl or 1-adamantyl carboxylate complexes are inert toward dioxygen, whereas the benzoate complex binds dioxygen at low temperature (<–20 °C). The adduct was identified as a μ-peroxo differic complex on the basis of the dioxygen uptake ($Fe:O_2 = 2:1$) and the spectral features (1) an intense absorption band at 682 nm attributable to a peroxide-to-iron charge transfer band, (2) ν(O–O) of 872 cm^{-1} which is typical for a peroxide ion bound to a transition metal ion, (3) antiferromagnetic interactions between ferric centers as ascertained by ^{1}H-NMR and variable temperature magnetic susceptibility, and (4) Fe···Fe separation of 4.3 Å estimated by EXAFS. The relatively weak antiferromagnetic property of the μ-peroxo complex in conjunction with the short Fe···Fe separation is accounted for by a unique Fe–O–O–Fe skeletal geometry: a dihedral angle of about 90° rather than 0° or 180°. While such a twisted μ-peroxo diferric complex is not presently known in biology, the present study clearly demonstrates that a coordinatively unsaturated ferrous complex with non-porphyrin environment consisting of N and O (carboxylate) ligand donors can effectively bind dioxygen. In this regard, the present system may serve as a functional mimic for hemerythrin and possibly for other non-heme iron proteins which bind or activate dioxygen. Steric bulk is clearly one of the important factors that enable a small synthetic molecule to bind dioxygen reversibly; this is also known for porphyrin complexes. While it has become apparent that the presence of a carboxylate ligand gives rise to isolable dioxygen iron complexes,[55] the rationale for this cannot be derived from the present study. To address this point more clearly, a series of ferrous complex $Fe(X)(HB(3,5\text{-}iPr_2)_3)$, where X denotes a potentially biologically relevant ligand, phenoxide, alkoxide, and thiolate, has been synthesized and their reactivities toward dioxygen are being investigated.

Experimental Section

Materials and Methods. Reagents and solvents were of commercially available reagent grade unless otherwise stated. Acetonitrile and toluene were carefully purified and reflux/distilled under argon from CaH_2 and sodium benzoquinone ketyl, respectively.[66] Preparation and handling of the complexes were performed under argon using standard Schlenk techniques. $KHB(3,5\text{-}iPr_2pz)_3$,[61] $KDB(3,5\text{-}iPr_2pz)_3$,[39] and $KHB(3,5\text{-}iPr_2\text{-}4\text{-}Brpz)_3$[39] were prepared by the methods described elsewhere.

Instruments. Infrared spectra were recorded as KBr pellets on a Hitachi 260-50 instrument. ^{1}H-NMR spectra were measured on either a JEOL EX-90 (90 MHz) or a JEOL GX-270 (270 MHz) NMR spectrometer. Chemical shifts are reported as δ values downfield from an internal standard Me_4Si. Electronic spectra were recorded on a Shimadzu UV-260 spectrometer. Low-temperature electronic spectra were obtained using an Oxford cryostats (DN1704). Field desorption mass spectra were recorded on a Hitachi M-80 mass spectrometer.

X-ray data were collected on a Rigaku AFC-5 four-circle diffractometer (AFC program package provided by Rigaku) equipped with a low-temperature apparatus. The structural analyses were carried out either by a FACOM A-70 computer with the CRYSTAN program package or by a MICRO-VAX II computer with the TEXSAN program package provided by Rigaku.

Raman spectra were obtained by excitation at 676 nm with a Kr^+ ion laser (Spectra Physics, 2016) and detected with an intensified photodiode array (PAR 1420HQ) attached to a double monochromator (Spex 1404).

---

(66) Perrin, D. D.; Armarego, W. L.; Perrin, D. R. *Purification of Laboratory Chemicals*, 2nd ed.; Pergamon: New York, 1980.

The data were processed with an OMA III system (PAR 1460). Raman shifts were calibrated with indene or CCl$_4$ as standard with an accuracy of ±1 cm^{-1}. All measurements were carried out with a spinning cell (diameter = 2 cm). the cell was spun at 1600 rpm in a cryostat that was cooled to -80 °C by flushing with cold N$_2$ gas. The laser power was lowered to the lowest possible (20 mW) to avoid photoreaction.

Variable temperature magnetic susceptibility data were acquired on an SHE 905 SQUID susceptometer at 10 kG using fine microcrystalline samples (30 mg) pressed into a precalibrated aluminum bucket. Samples were also run at 2 kG to check for ferromagnetic impurities. Consistency of μ_{eff} at both fields to within 2% showed the absence of significant ferromagnetic impurities. Thermally unstable compounds were loaded at -70 °C by a technique to be described elsewhere.[67] Since the thermally unstable compounds had to be weighed at room temperature after measurement, and since possible solvent occlusion cannot be rigorously taken into account, there is a greater uncertainty in the absolute magnetic susceptibility than might normally be expected. There is, however, no reason to believe this amounts to more than a few percent, because eventual weight loss of the samples (by ~5%) required 30 min at ambient conditions. Theoretical fits to the susceptibility data were optimized within the framework of standard spin Hamiltonian treatment ($-2J$) using programs supplied by Dr. P. D. W. Boyd. Fitting parameters are given in the Figure 9 caption. Diamagnetic corrections were calculated from Pascal constants and allowed to vary by up to 15% in the fits ($\Delta\chi_{diam}$). Data for the dioxygen adduct of Fe(OBz)(HB(3,5-iPr$_2$pz)$_3$) are given in Table S2 of the supplementary material.

Mössbauer spectra were recorded on powder samples at room temperature on Ranger Scientific equipment set up at the University of Southern California by Tom Kent of WEB Research who also supplied the software for data analysis. Isomer shifts are relative to iron foil at room temperature.

Fe(OAc)(HB(3,5-iPr$_2$pz)$_3$) (2). The ferrous chloro complex **1** (498 mg; 0.89 mmol) was stirred overnight with a slightly excess amount of NaOAc (113 mg; 1.38 mmol) in a mixture of 20 mL of toluene and 5 mL of MeCN. The formed precipitate was removed by filtration, and the filtrate was dried under vacuum, resulting in a white solid. The solid was dissolved in 5 mL of pentane. After filtration, the solution was concentrated under vacuum and cooled at -20 °C overnight, affording **2** as colorless needles (457 mg, 88%): ^{1}H-NMR (toluene-d_8, 270 MHz, 27 °C) - 6.8 (s, 1H, B*H*), -3.1 (s, 18H, CH*Me*$_2$), 4.0 (s, 18H, CH*Me*$_2$), 9.8 (s, 3H, C*H*Me$_2$), 14.4 (s, 3H, C*H*Me$_2$), 62.8 (s, 3H, pz), 111.8 (s, 3H, OAc); IR (cm^{-1}) ν(BH) 2535, ν_{as}(COO) 1562, ν_s(COO) 1429. Anal. Calcd for C$_{29}$H$_{49}$N$_6$BO$_2$Fe: C, 60.01; H, 8.51; N, 14.48. Found: C, 59.64; H, 8.84; N, 14.92.

Fe(OBz)(MeCN)(HB(3,5-iPr$_2$pz)$_3$) (3). In a 50 mL Schlenk tube, 0.771 g (1.39 mmol) of **1** and 0.307 g (2.12 mmol) of NaOBz were reacted in a mixture of 30 mL of toluene and 5 mL of MeCN for 1 day. After filtration, the filtrate was dried under vacuum, yielding a yellow powder. The solid was dissolved in 10 mL of MeCN and cooled at -20 °C overnight, to afford **3** as yellow needles (0.834 g; 88 %): ^{1}H-NMR (toluene-d_8, 270 MHz, 27 °C) -9.1 (s, 1H, B*H*), -1.8 (s, 18H, CH*Me*$_2$), 0.8 (s, 3H, *Me*CN), 1.6 (s, 1H, *p*-Ph), 3.7 (s, 18H, CH*Me*$_2$), 8.9 (s, 2H, *m*-Ph), 11.3 (br, 5H, C*H*Me$_2$ and *o*-Ph), 13.7 (s, 3H, C*H*Me$_2$), 63.9 (s, 3H, pz); IR (cm^{-1}) ν(BH) 2526, ν(CN) 2277, ν(Ph) 1598, ν_{as}(COO) 1536, ν_s(COO) 1418. Anal. Calcd for C$_{36}$H$_{54}$N$_7$BO$_2$Fe: C, 60.33; H, 7.45; N, 12.42. Found: C, 60.06; H, 7.45; N, 12.33.

Fe(OBz)(HB(3,5-iPr$_2$pz)$_3$) (4). The MeCN in **3** is easily removed when evacuated under vacuum. Thus, **3** was evacuated for 6 h, and then the resulting solid was recrystallized from pentane: ^{1}H-NMR (benzene-d_6, 270 MHz, 27 °C) -9.5 (s, 1H, B*H*), -1.5 (s, 18H, CH*Me*$_2$), 1.8 (s, 1H, *p*-Ph), 3.7 (s, 18H, CH*Me*$_2$), 9.1 (s, 2H, *m*-Ph), 11.7 (br, 5H, C*H*Me$_2$ and *o*-Ph), 13.3 (s, 3H, C*H*Me$_2$), 63.2 (s, 3H, pz); IR(cm^{-1}) ν(BH) 2535, ν(Ph) 1595, ν_{as}(COO) 1536, ν_s(COO) 1418. Anal. Calcd for C$_{34}$H$_{51}$N$_6$BO$_2$Fe: C, 63.56; H, 8.00; N, 13.08. Found C, 63.72; H, 8.11; N, 13.12.

Fe(OBz)(HB(3,5-iPr$_2$-4-Brpz)$_3$) (5). Complex **5** was prepared by the method applied for **4** with KHB(3,5-iPr$_2$-4-Brpz)$_3$: ^{1}H-NMR (benzene-d_6, 90 MHz, 25 °C) 1.3 (s, 18H, CH*Me*$_2$), 3.9 (s, 1H, Ph), 4.5 (s, 18H, CH*Me*$_2$), 10.7 (s, 2H, Ph), 12.2 (s, 3H, C*H*Me$_2$), 15.2 (s, 3H, C*H*Me$_2$). Anal. Calcd for C$_{34}$H$_{48}$N$_6$BBr$_3$O$_2$Fe: C, 46.45; H, 5.50; N, 9.56; Br, 27.27. Found: C, 46.07; H, 5.55; N, 9.91; Br, 26.70.

Fe(OOCC$_6$H$_4$-*p*-NO$_2$)(HB(3,5-iPr$_2$pz)$_3$) (6). Complexes **6–11** were obtained in a similar manner applied to **3**. The samples used for the experiments were evacuated under vacuum extensively: Yield 67%; ^{1}H-NMR (toluene-d_8, 270 MHz, 27 °C) -13.8 (s, 1H, B*H*), -0.4 (s, 18H, CH*Me*$_2$), 3.0 (s, 18H, CH*Me*$_2$), 8.7 (s, 2H, *m*-Ph), 9.0 (s, 2H, *o*-Ph), 12.5 (s, 3H, C*H*Me$_2$), 14.9 (s, 3H, C*H*Me$_2$), 64.3 (s, 3H, pz); IR (cm^{-1}) ν(BH) 2553, ν(Ph) 1618, ν_{as}(COO) 1559, ν_s(COO) 1427, ν(NO$_2$) 1345. Anal. Calcd for C$_{34}$H$_{50}$N$_7$BO$_4$Fe: C, 59.40; H, 7.33; N, 14.26. Found: C, 59.43; H, 7.35; N, 14.17.

Fe(OOCC$_6$H$_4$-*p*-NO$_2$)(DB(3,5-iPr$_2$pz)$_3$) (7): ^{1}H-NMR (benzene-d_6, 270 MHz, 27 °C) -0.3 (s, 18H, CH*Me*$_2$), 2.9 (s, 18H, CH*Me*$_2$), 8.8 (s, 2H, Ph), 9.0 (s, 2H, Ph), 12.2 (s, 3H, C*H*Me$_2$), 15.7 (s, 3H, C*H*Me$_2$), 65.3 (s, 3H, pz).

Fe(OOCC$_6$H$_4$-*p*-Cl)(HB(3,5-iPr$_2$pz)$_3$) (8): Yield 21%; ^{1}H-NMR (toluene-d_8, 270 MHz, 27 °C) -10.7 (s, 1H, B*H*), -1.1 (s, 18H, CH*Me*$_2$), 3.6 (s, 18H, CH*Me*$_2$), 8.6 (s, 2H, *m*-Ph), 10.4 (s, 2H, *o*-Ph), 12.4 (s, 3H, C*H*Me$_2$), 13.4 (s, 3H, C*H*Me$_2$), 63.8 (s, 3H, pz); IR (cm^{-1}) ν(BH) 2540, ν(Ph) 1590, ν_{as}(COO) 1536, ν_s(COO) 1423. Anal. Calcd for C$_{34}$H$_{50}$N$_6$BClO$_2$Fe: C, 60.33; H, 7.45; N, 12.24; Cl, 5.24. Found, C, 60.52; H, 7.77; N, 12.85; Cl, 5.53.

Fe(OOCC$_6$H$_4$-*p*-F)(HB(3,5-iPr$_2$pz)$_3$) (9): Yield 25%; ^{1}H-NMR (benzene-d_6, 90 MHz, 25 °C) -9.5 (s, 1H, B*H*), -1.2 (s, 18H, CH*Me*$_2$), 3.8 (s, 18H, CH*Me*$_2$), 7.6 (s, 2H, *m*-Ph), 8.4 (s, 2H, *o*-Ph), 11.2 (s, 3H, C*H*Me$_2$), 13.6 (s, 3H, C*H*Me$_2$), 64.1 (s, 3H, pz); IR (cm^{-1}) ν(BH) 2538, ν(Ph) 1601, ν_{as}(COO) 1536, ν_s(COO) 1425. Anal. Calcd for C$_{34}$H$_{50}$N$_6$BFO$_2$Fe: C, 61.83; H, 7.63; N, 12.72; F, 2.88. Found: C, 61.30; H, 7.60; N, 12.56; F, 2.83.

Fe(OOCC$_6$H$_4$-*p*-Me)(HB(3,5-iPr$_2$pz)$_3$) (10): Yield 48%; ^{1}H-NMR (toluene-d_8, 270 MHz, 27 °C) -8.5 (s, 1H, B*H*), -1.9 (s, 18H, CH*Me*$_2$), 3.8 (s, 18H, CH*Me*$_2$), 8.1 (s, 3H, *p-Me*), 9.0 (s, 2H, *m*-Ph), 10.2 (s, 3H, C*H*Me$_2$), 11.7 (s, 3H, *o*-Ph), 13.8 (s, 3H, C*H*Me$_2$), 63.0 (s, 3H, pz); IR (cm^{-1}) ν(BH) 2528, ν(Ph) 1595, ν_{as}(COO) 1531, ν_s(COO) 1420. Anal. Calcd for C$_{35}$H$_{53}$N$_6$BO$_2$Fe: C, 64.03; H, 8.14; N, 12.80. Found: C, 64.46; H, 7.94; N, 12.82.

Fe(OOCC$_6$H$_4$-*p*-NH$_2$)(HB(3,5-iPr$_2$pz)$_3$) (11): Yield 86.0 %; ^{1}H-NMR (toluene-d_8, 270 MHz, 27 °C) -5.3 (s, 1H, B*H*), -3.0 (s, 18H, CH*Me*$_2$), 3.9 (s, 2H, N*H*$_2$), 4.2 (s, 18H, CH*Me*$_2$), 7.0 (s, 3H, C*H*Me$_2$), 8.4 (s, 2H, *m*-Ph), 13.3 (s, 2H, *o*-Ph), 14.7 (s, 3H, C*H*Me$_2$), 62.4 (s, 3H, pz); IR (cm^{-1}) ν(NH$_2$) 3486, 3389, ν(BH) 2541, ν(Ph) 1606, ν_{as}(COO) 1513, ν_s(COO) 1414. Anal. Calcd for C$_{34}$H$_{52}$N$_7$BO$_2$Fe: C, 62.11; H, 7.97; N, 14.91. Found: C, 62.05; H, 7.79; N, 14.87.

Fe(OOCAd)(HB(3,5-iPr$_2$pz)$_3$) (12). Complex **1** (0.616 g, 1.11 mmol) was reacted with NaOOCAd (OOCAd denotes 1-adamantylcarboxylate) (0.348 g, 1.72 mmol) in a mixed solvent (25 mL of toluene and 5 mL of MeCN) for 2 days. After filtration, the filtrate was dried under vacuum. Recrystallization of the resulting solid from MeCN yielded **12** as white needles (0.749 g, 96 %): ^{1}H-NMR (benzene-d_6, 270 MHz, 25 °C) -14.0 (s, 1H, B*H*), -4.5 (s, 18H, CH*Me*$_2$), -2.2 (s, 6H, Ad), 4.5 (s, 18H, CH*Me*$_2$), 4.8 (s, 6H, Ad), 13.1 (s, 3H, C*H*Me$_2$), 15.2 (s, 3H,C*H*Me$_2$), 48.8 (s, 3H, Ad), 63.3 (s, 3H, pz); IR (cm^{-1}) ν(BH) 2542, ν_{as}(COO) 1542, ν_s(COO) 1432. Anal. Calcd for C$_{38}$H$_{61}$N$_6$BO$_2$Fe: C, 65.15; H, 8.78; N, 12.00. Found: C, 64.72; H, 8.49; N, 12.26.

Fe(OOCtBu)(HB(3,5-iPr$_2$pz)$_3$) (13). Complex **1** (276 mg, 0.50 mmol) was stirred with NaOOCtBu (91 mg, 0.74 mmol) in a mixture of 13 mL of toluene and 3 mL of MeCN overnight. After removal of the precipitate, the filtrate was evacuated under vacuum to dryness. The resulting white solid was recrystallized from 5 mL of pentane at -20 °C, affording **13** as a white solid (158 mg, 51 %): ^{1}H-NMR (toluene-d_8, 270 MHz, 27 °C) -4.3 (s, 18H, CH*Me*$_2$), 4.4 (s, 18H, CH*Me*$_2$), 13.5 (s, 9H, tBu), 15.2 (s, 3H, C*H*Me$_2$), 63.2 (s, 3H, pz); IR (cm^{-1}) ν(BH) 2535, ν_{as}(COO) 1533, ν_s(COO) 1425. Anal. Calcd for C$_{32}$H$_{55}$N$_6$BO$_2$Fe: C, 61.74; H, 8.91; N, 13.50. Found: C, 61.35; H, 9.07; N, 13.45.

Fe(OOCEt)(HB(3,5-iPr$_2$pz)$_3$) (14). Complex **1** (460 mg, 0.83 mmol) was reacted with 1.5 equiv of NaOOCEt (121 mg, 1.26 mmol) in a toluene/MeCN mixture (20 mL/5 mL) overnight. After filtration, the filtrate was dried under vacuum and the resulting solid was recrystallized from pentane at -20 °C, yielding **14** as white solid (374 mg, 76%): ^{1}H-NMR (toluene-d_8, 270 MHz, 27 °C) -6.5 (s, 1H, B*H*), -3.4 (s, 18H, CH*Me*$_2$), 4.2 (s, 18H, CH*Me*$_2$), 6.3 (s, 3H, CH$_2$C*H*$_3$), 9.0 (s, 3H, C*H*Me$_2$), 14.8 (s, 3H, C*H*Me$_2$), 64.2 (s, 3H, pz), 101.1 (s, 2H, C*H*$_2$CH$_3$); IR (cm^{-1}) ν(BH) 2536, ν_{as}(COO) 1535, ν_s(COO) 1428. Anal. Calcd for C$_{30}$H$_{51}$N$_6$BO$_2$Fe: C, 60.62; H, 8.65; N, 14.14. Found: C, 60.37; H, 8.56; N, 14.15.

Fe(OOCiPr)(HB(3,5-iPr$_2$pz)$_3$) (15). This complex was prepared in the same manner as **14**: Yield 65%; ^{1}H-NMR (toluene-d_8, 270 MHz, 27 °C) -7.4 (s, 1H, B*H*), -2.7 (s, 18H, CH*Me*$_2$), 3.9 (s, 18H, CH*Me*$_2$), 8.1 (s, 6H, CCH*Me*$_2$), 13.3 (s, 3H, C*H*Me$_2$), 61.5 (s, 3H, pz), 85.7 (s, 1H, CC*H*Me$_2$); IR (cm^{-1}) ν(BH) 2532, ν_{as}(COO) 1535, ν_s(COO) 1428.

---

(67) Mathur, R.; Heerwegh, K.; Reed, C. A. To be submitted to *Inorg. Chem.*

Table 8. Crystallographic details of **2**, **3**, **13**, and **16**·6C_7H_8

complex	**2**	**3**	**13**	**16**·6C_7H_8
formula	$C_{29}H_{49}N_6O_2BFe$	$C_{36}H_{54}N_7O_2BFe$	$C_{32}H_{55}N_6O_2BFe$	$C_{124}H_{161}N_{12}O_{10}B_2Fe_3$
formula weight	580.41	683.53	622.49	2168.88
crystal system	monoclinic	monoclinic	monoclinic	orthorhombic
space group	$P2_1/n$	$P2_1/n$	$C2/c$	$Pccn$
a (Å)	15.798(2)	26.007(10)	35.208(3)	20.107(6)
b (Å)	16.840(3)	15.320(3)	9.465(2)	25.386(6)
c (Å)	12.431(2)	9.936(3)	24.403(3)	25.059(7)
β (deg)	97.80(2)	93.93(2)	114.619(7)	
V (Å^3)	3276.4(9)	3950(2)	7393(4)	12791(6)
Z	4	4	8	4
D(calcd) (g cm^{-3})	1.18	1.15	1.12	1.13
crystal size (mm)	0.6 × 0.3 × 0.2	0.5 × 0.3 × 0.2	0.6 × 0.5 × 0.3	0.8 × 0.8 × 0.7
data collection temp. (°C)	−60	20	20	−50
radiation	graphite-monochromatized Mo Kα (0.710 68 Å)			
μ(Mo Ka) (cm^{-1})	4.90	4.17	4.39	3.90
scan mode	$\omega - 2\theta$	ω	$\omega - 2\theta$	$\omega - 2\theta$
scan width (deg)	1.30 + 0.14 tan θ	1.30 + 0.14 tan θ	1.17 + 0.14 tan θ	1.30 + 0.14 tan θ
2θ range	3–50	2–55	5–50	3–50
octant measure	$\pm h,k,l$	$\pm h,k,l$	$h,k,\pm l$	h,k,l
no. of measured reflections	6291	10255	7212	12390
no. of observed reflections	4518 ($F_o \geq 3\sigma(F_o)$)	4075 ($F_o \geq 3\sigma(F_o)$)	4330 ($F_o \geq 6\sigma(F_o)$)	5356 ($F_o \geq 3\sigma(F_o)$)
R (%)	7.03	8.97	3.96	12.2
R_w (%)	7.53	9.15	5.46	14.8

Anal. Calcd for $C_{31}H_{53}N_6BO_2Fe$: C, 61.19; H, 8.78; N, 13.81. Found: C, 60.83; H, 8.65; N, 13.53.

Irreversible Oxygenation of 4 to (HB(3,5-iPr$_2$pz)$_3$)Fe(OBz)$_2$(O)Fe(OH)(OBz)$_2$Fe(HB(3,5-iPr$_2$pz)$_3$) (16). Ferrous benzoato complex **4** (268 mg, 0.42 mmol) was exposed to 1 atm dioxygen for 1 h in toluene at −78 °C, resulting in bluish green colored solution. The solution was allowed to stand at −20 °C overnight. Toluene was removed by evaporation, and the resulting solid was recrystallized from toluene. Complex **16** was obtained as dark green crystals suitable for X-ray diffraction (127 mg, 19% yield based on **4**): FD-MS 1494 (**16** − PhCOOH); IR (cm^{-1}) ν(OH) 3632, ν(BH) 2543, ν(Ph) 1595, ν_{as}(COO) 1573, ν_s(COO) 1391; UV-vis (in CH_2Cl_2, nm, ϵ, M^{-1} cm^{-1}) 375 (16 400), 490 (1820), 615 (300); Mössbauer ΔE_q = 1.45, δ = 0.49 mm sec^{-1}, rel area 0.67; ΔE_q = 0.6, δ = 0.1 mm sec^{-1}, rel area 0.32). Anal. Calcd for $C_{82}H_{114}N_{12}N_{12}B_2O_{10}Fe_3$: C, 60.95; H, 7.05; N, 10.40. Found: C, 60.83; H, 7.26; N, 10.41.

Isolation of the Dioxygen Adduct of 4. In 10 mL of pentane, 0.218 g of **4** was dissolved under argon. The atmosphere was replaced with dioxygen and the solution was allowed to stand at −78 °C, causing precipitation of the dioxygen adduct as a microcrystalline dark green solid.

X-ray Data Collections and Structural Analyses. Single crystals of **2** and **13** were obtained by recrystallization at −20 °C from pentane. The single crystals of **4** and **16** were prepared from MeCN and toluene, respectively. Complex **16** was crystallized as a solvated form **16**·6C_7H_8. The crystals were sealed in thin-walled glass capillaries. The data for **4** and **13** were recorded at room temperature, while the data collection for **2** and **16**·6C_7H_8 were carried out −60 and −50 °C, respectively. A Mo X-ray source equipped with a graphite monochromator (Mo Kα, λ = 0.710 68 Å) was used. Automatic centering and least-squares routines were carried out for all compounds with 25 reflections of 25 ° ≤ 2Θ ≤ 30° to determine the cell parameters (AFC program from Rigaku). All data were corrected for Lorentz and polarization effects but not absorption. The intensities of three standard reflections monitored every 100 reflections showed no serious decay. A summary of cell parameters, data collection conditions, and refinement results for **2**, **4**, **13**, and **16**·6C_7H_8 are given in Table 8.

The initial positional parameters of the iron atom in **2** and **4** were determined by the direct method SAPI85. The positional parameters of the iron atoms in **13** and **16**·6C_7H_8 were obtained by the direct method MITHRIL. Subsequent difference Fourier synthesis easily located all non-hydrogen atoms, which were refined anisotropically by CRYSTAN for **2** and **4** and by TEXSAN for **13** and **16**·6C_7H_8. The hydrogen atoms except on methyl groups were calculated and included in the final refinement for **2** and **4**. The hydrogen atoms on the methyl groups were not included for the refinement. All hydrogen atoms except those on the solvent molecules were calculated and isotropically fixed in the final refinement cycles for **13** and **16**·6C_7H_8. The high disorder of solvent molecules in **16**·C_7H_8 was evident so the locations of the disordered solvent atoms could not be accurately determined, which resulted in the relatively large residual for **16**·6C_7H_8. The final R and R_w factors are given in Table 8, where $R = \sum (|F_o| - |F_c|)/\sum|F_o|$ and $R_w = [\sum[w(|F_o| - |F_c|)^2/\sum w|F_o|^2]^{1/2}$ with $w = 1/\sigma^2(F_o^2)$.

Full bond distances, bond angles, and anisotropic thermal parameters of non-hydrogen atoms, hydrogen atom coordinates, and F_o/F_c tables for **2**, **4**, **13**, and **16**·6C_7H_8 are available as supplementary material.

EXAFS Data Collection and Analysis. X-ray absorption spectra (XAS) were collected between 6.9 and 8.1 keV at station C2 of the Cornell High Energy Synchrotron Source (CHESS) and at beamline X9A of the National Synchrotron Light Source (NSLS) at Brookhaven National Laboratory. The monochromator was calibrated by using the 1s → 3d feature at 7113.0 eV in the XAS spectrum of $(Et_4N)[FeCl_4]$. The XAS data for Fe(OBz)(HB(3,5-iPr$_2$pz)$_3$) (**4**) were obtained in transmission mode ($A_{exp} = -\log_{10}I_t/I_0$) as a dispersion of the microcrystalline solid in boron nitride (Aldrich, Milwaukee, WI) at room temperature. The data for the dioxygen adduct of **3** were obtained in fluorescence mode as frozen toluene solutions at 77 K. $A_{exp}(C_f/C_0)$ was determined from an incident (C_0) ionization detector and a final fluorescence (C_f) detector. A large solid-angle Lytle fluorescence detector was used with an Mn filter and Soller slits.[68]

The treatment of the raw EXAFS data to yield X is discussed at length in several review articles.[69,70] Details of our data treatment procedure including correction of fluorescence data for thickness effects and detector response, have been presented previously.[71] The refinements reported were of RMS$_{dev}$/RMS$_{dat}$ of k^3X data, and the function minimized was $R \equiv [\sum k^6(X_c - X)^2/n]^{1/2}$, where the sume is over n data points between 2 and 14 Å^{-1}.[71]

(a) Use of Theoretical Phase and Amplitude Functions. Single-scattering EXAFS theory allows each shell of n scatterers to be molded separately, with the EXAFS spectrum described as a sum of each shell[71]

$$X_c = \sum\nolimits_{\text{shells}} nA[f(k)k^{-1}r^{-2}\exp(-2\sigma^2k^2)\sin[2kr + \alpha(k)]] \quad (7)$$

where $k = [8\pi^2m_e(E - E_0 + \Delta E)/h^2]^{1/2}$. The amplitude reduction factor (A) and the shell-specific edge shift (ΔE) are empirical parameters that partially compensate for imperfections in the theoretical ampritude and phase functions f and α.[72] These empirical parameters are derived from the EXAFS analysis of crystallographically characterized model complexes, such as Fe(acac)$_3$.

Our analysis procedure, a variation of FABM ("fine adjustment based on models"),[73] uses theoretical phase and amplitude functions calculated using a curved-wave formalism. For each shell, crystallographically characterized model complexes are used to determine A and ΔE.[72] This

---

(68) Stern, E. A.; Heald, S. M. *Rev. Sci. Instrum.* **1979**, *50*, 1579.

(69) Teo, B.-K. In *EXAFS Spectroscopy, Techniques and Applications*; Teo, B.-K., Joy, D. C., Eds.; Plenum: New York, 1981; p 13.

(70) Scott, R. A. *Methods Enzymol.* **1985**, *117*, 414.

(71) Scarrow, R. C.; Maroney, M. J.; Palmer, S. M.; Que, L., Jr.; Roe, A. L.; Salowe, S. P.; Stubbe, J. *J. Am. Chem. Soc.* **1987**, *109*, 7857.

(72) Teo, B.-K.; Lee, P. A. *J. Am. Chem. Soc.* **1979**, *101*, 2815.

leaves two parameters per shell (r and n or σ^2) to be refined instead of the four parameters refined using BFBT ("best fit based on theory").[73]

Recent studies have indicated that the single-scattering EXAFS theory is valid to lower energies than previously believed.[74,75] However, the amplitude and phase function tables of Teo and Lee[72] were calculated using a plane wave approximation for the scattering of the photoelectron wave by the neighboring atom and are satisfactory at low photoelectron momentum. Recently, McKale et al.[76] have calculated amplitude and phase shift functions for $2 \le k \le 20$ Å^{-1} using a spherical wave formalism, thus extending the range of EXAFS data that can be used in refinement to $k = 2$ Å^{-1}. Use of these "curved-wave" functions has consistently yielded better fits than those determined with the Teo–Lee tables. However, using data at low photoelectron momentum raises the question of whether other effects such as XANES may be contributing to the EXAFS spectrum. However, in both model compounds and proteins, analysis of the data in the range $2 \le k \le 14$ Å^{-1} gave identical fits to those using data in the range $3 \le k \le 14$ or even $4 \le k \le 14$. Thus, it can be assumed that contributions from phenomena other than EXAFS are negligible in the k range ($2 \le k \le 14$ Å^{-1}) used in the fits presented here.

(b) Integration of the 1s → 3d Peak. The preedge areas in the XANES data were calculated by subtracting an arctangent function from the data and normalizing with respect to the edge jump height. The background function was determined by a least-squares fit of an arctangent together with a first-order polynomial to the data below the inflection point as previously described.[50] The area of the preedge peak after the background subtraction was obtained by integrating over a range of ~8 eV. This range centered on the peak and any residual background function was interpolated over that range. The edge jump was determined by fitting first-order polynomials to the data as previously described.[50] The difference between these two lines at the inflection point of the edge was used as the normalization factor for the preedge peak area. For example, one of the samples of the O_2 adduct of [LFe(OBz)] had a normalized preedge peak area of 4.7×10^{-2} eV, which is abbreviated as 4.7 units.

Molecular Orbital Calculations. Extended Hückel calculations were used, with a weighted H_{ij} formula.[77] The atomic parameters for Fe were taken from previous calculations[78] as follows: (H_{ii}) 4s, −9.17 eV; 4p, −5.37 eV; 3d, −12.7 eV; (orbital exponents) 4s, 1.9p 4p, 1.9; 3d, 5.35(0.5366) + 1.80(0.6678). The C, N, O, and H parameters are the standard ones. The geometrical parameters of the model complexes were the following: Fe–O, 1.80 Å; O–O, 1.45 Å; Fe–H, 1.80 Å; NH_3 group, tetrahedral; N–H, 1.0 Å; Fe–O (OOCH), 2.2 Å; O–Fe–O (OOCH), 60°; O–C, 1.25 Å, C–H, 1.08 Å.

Acknowledgment. We thank Dr. M. Tanaka of Tokyo Institute of Technology for kind help in refining the X-ray structure of **16**·$6C_7H_8$. We also thank Drs. Richard Holz and Anne True for assistance with EXAFS data collection. We would especially like to thank Dr. Syed Khalid of the Biostructures PRT at beamline X9A of the NSLS and the operators at CHESS for their help. Support for this research from the Ministry of Education, Science and Culture, Japan (04453044 and 04225107) is gratefully acknowledged. This work was partly supported by the NIH (L.Q., GM33162 and C.A.R., GM23581). C.R.R. is grateful for a Predoctoral Traineeship from the U.S. Public Hewalth Service (T32GM07323-16) and K.H. thanks the U.S. Department of Education for support (GAANN fellowship).

Supplementary Material Available: Plot of $1/(\delta - \delta_2)$ vs [Py] (Figure S1), plot of k^3-weighted data (- -) and multishell fits (—) of Fe(OBz)(HB(3,5-iPr_2pz)$_3$) and [Fe(OBz)(HB(3,5-iPr_2pz)$_3$)]$_2$(O_2) Figure S2, Model of [Fe(OBz)(HB(3,5-iPr_2pz)$_3$)]$_2$(O_2) as in Figure 12, but with isopropyl groups shown (Figure S3), X-ray experimental for **2**, **4**, **11**, and **16**·$6C_7H_8$ (Figure S4), crystal data and collection details (Figure S5), atomic numbering (Figure S6), atomic coordinates including hydrogen atoms and isotropic thermal parameters (Figure 7), anisotropic thermal parameters (Figure S8), bond distances (Figure S9), bond angles (Figure S10), Table S1: complete multishell fits of Fe(OBz)(HB(3,5-iPr_2pz)$_3$) and its dioxygen adduct (Table S1), and SQUID data for [Fe(OBz)(HB(3,5-iPr_2pz)$_3$)]$_2$(O_2) (Table S2) (48 pages); observed and calculated structure factors (Figure S11) (93 pages). This material is contained in many libraries on microfiche, immediately follows this article in the microfilm version of the journal, and can be ordered from the ACS; see any current masthead page for ordering information.

---

[73] Teo, B.-K.; Antonio, M. R.; Averill, B. A. *J. Am. Chem. Soc.* **1983**, *105*, 3751.

[74] Bunker, G. B.; Stern, E. A. *Phys. Rev. Lett.* **1984**, *52*, 1990.

[75] Müller, J. E.; Schaich, W. L. *Phys. Rev. B* **1983**, *27*, 6489.

[76] McKale, A. G.; Veal, B. W.; Paulikas, A. P.; Chan, S.-K.; Knapp, G. S. *J. Am. Chem. Soc.* **1988**, *110*, 3763.

[77] Hoffmann, R. *J. Chem. Phys.* **1963**, *39*, 1397.

[78] (a) Tatsumi, K.; Yasuda, H.; Nakamura, A. *Isr. J. Chem.* **1983**, *23*, 145. (b) Summerville, R. H.; Hoffmann, R. *J. Am. Chem. Soc.* **1976**, *98*, 7240.